# High-Frequency 12 V Regulated *LLC* Bus Converter With Integrated Multiphase Inverse Coupled Resonant Inductor

Lei Wang, Donglai Zhang, *Senior Member, IEEE*, Jinpei Duan, and Yangyang Hao

***Abstract*—In the application of 48 V bus converter, the traditional multiphase regulated *LLC* converter has some shortcomings, such as insufficient gain range, low light-load efficiency, and difficult current sharing. In order to improve the performance, this article investigates a comprehensive design scheme of multiphase interleaved magnetic integrated *LLC* converter, which can extend the gain range and achieve active current sharing simultaneously. First, a new structure of multiphase inverse coupled resonant inductor and magnetic integrated transformer is proposed. Then, a high-precision magnetic circuit model is constructed to optimize the design of integrated inductor and transformer. On this basis, the three-phase interleaved magnetic-integrated *LLC* converter prototype is manufactured, which has a 36–75 V input voltage range and a 12 V regulated output voltage. In addition, the prototype can output 1080 W power in a quarter brick and has a power density of 716 W/in$^3$. The maximum efficiency at rated input voltage is 97.5% and remains above 96% over the main input voltage range. As shown by the quantitative performance comparison results, the proposed converter is superior to other state-of-the-art solutions in terms of the comprehensive performance.**

***Index Terms*—Current sharing, high-efficiency and high-power density, interleaved magnetic integration, inverse coupled inductor, *LLC* converter.**

## I. Introduction

LLC converter is widely applied to aviation power supply, dc microgrid, electric vehicle charging, data center, and telecommunication server and other fields due to the advantages of high-efficiency, high-power density, simple structure, simple control strategy, and good electromagnetic compatibility characteristics [1], [2], [3], [4]. Meanwhile, a wider range of applications also has more requirements for *LLC* converters, including the ability to adapt to a wide voltage range, the characteristics of fast dynamic response and low ripple output, high efficiency and small size in high-current applications, etc. However, when the structure and control method of the traditional *LLC* converter meet these requirements, the performance of the converter will always be affected [5]. Many studies have been carried out in order to make the *LLC* converter suitable for wide input voltage [6], [7], [8], [9], [10], [11], [12], [13], [14], [15], [16], [17], [18], [19].

The traditional solution is to use two-stage structure converter [6], [7]. The input and output voltage can be easily adjusted in a wide range by connecting the *LLC* converter in series with the voltage regulation module. At the same time, each stage of the converter can be easily optimized. However, the two-stage and quasi single-stage structure inevitably leads to the low efficiency and power density.

Through improvement of the traditional *LLC* topology, good results have been achieved in making the voltage gain characteristics better for wide input voltage applications [8], [9], [10], [11]. The solution reported in [8] introduces *LCLC* resonant topology from the perspective of improving voltage gain. The converter proposed in [9] adds an additional *LC* resonant structure, which shows the characteristics of variable inductor at different switching frequencies and, thus, makes the converter more suitable for applications in wide input voltage range. Besides, Inam et al. [10] proposed an *LLC* converter using resistance compression network, which can realize soft switching in a wide range of input voltage. In [11], a four-element resonant converter was proposed. The voltage gain curve of it contains a unique voltage gain zero so that the ability to regulate voltage in a wide range is obtained. In addition, Sun et al. [12], [13], [14] combined interleaving boost inductor, auxiliary winding, and *LC* filter with traditional *LLC* converter to achieve high efficiency under wide voltage input.

In the above studies [8], [9], [10], [11], [13], [14], the efficiency and voltage gain of *LLC* have been improved more or less by improving the topology. However, they all have a fixed structure and can merely improve a certain performance of the converter in a specific situation, which results in limited application. In order to deal with this problem, a series of multimode *LLC* converters have been proposed [15], [16], [17], [18], [19]. Hu et al. [15] proposed an improved *LLC* converter serial connected with double transformer, which expanded the voltage gain range by mode switching. Moreover, Wang et al.

Manuscript received 9 December 2021; revised 13 July 2022 and 4 November 2022; accepted 13 December 2022. Date of publication 29 December 2022; date of current version 10 March 2023. This work was supported in part by the National Key Research and Development Program of China under Grant 2020YFC2201000 and in part by Shenzhen Science and Technology Plan Project under Grant JSGG20200701095208014. Recommended for publication by Associate Editor Q. Li. *(Corresponding author: Donglai Zhang.)*

The authors are with the Power Electronic and Motion Control Research Center, Harbin Institute of Technology (Shenzhen), Shenzhen 518000, China (e-mail: 975743670@qq.com; zhangdonglai@hit.edu.cn; 497794969@qq.com; haoyangyang520@163.com).

Color versions of one or more figures in this article are available at https://doi.org/10.1109/TPEL.2022.3232893.

Digital Object Identifier 10.1109/TPEL.2022.3232893

[16] discussed a kind of *LLC* converter that can increase the voltage gain by auxiliary switch. The *LLC* converter proposed in [17] can switch flexibly between full-bridge structure and half-bridge structure so that a wide voltage gain can be obtained in a narrow operating frequency range. Besides, Shahzad et al. [18] presented a staggered *LLC* converter with dual voltage rectifier in series for charging PEV batteries. Furthermore, Jin and Ruan [19] proposed a compound full-bridge three-level *LLC* converter, which can improve the gain by switching between three-level and two-level modes. The above schemes [15], [16], [17], [18], [19] reconstruct the topology structure and working mode through software control so as to make the *LLC* converter work efficiently in a wide voltage range. Their main drawback is the complexity of control, and the transient process of switching *LLC* topology mode directly will inevitably affect the stability of the converter.

Multiphase interleaved *LLC* converter is usually used in large current occasions, but the current sharing of all phases must be guaranteed. Hu et al. [20] adopted frequency modulation control and Murata and Kurokawa [21] used phase-shifting control, both of which can achieve good current sharing. However, the main disadvantages are additional sampling circuit, high cost, and complex control. Additionally, Wang et al. [22] proposed a series input structure that can directly improve current sharing. In [23], an improved resonant network structure was put forward to achieve current sharing, which can be extended to *LLC* with more phases. What is more, Yang et al. [24] proposed the method of grouping secondary-side windings to achieve better automatic current sharing, but this method is mainly suitable for the application of two-phase *LLC*. In [25] and [26], printed circuit board (PCB) winding and magnetic integration design were adopted for the multiphase interleaved *LLC* to further reduce core loss and improve power density, but the connection modes are only applicable for the three-phase converter and cannot extend the number of working phases.

To sum up, the published article is only aimed to optimize a certain performance of *LLC* converter; up to now, the multiphase regulated *LLC* converter, which can achieve automatic current sharing, improve the voltage gain, power density, and effectiveness, has not been found. Also, its comprehensive design and experimental solution have not been found, which severely impede the development of multiphase interleaved *LLC* converter applications. To solve this problem, based on the previous studies [6], [7], [8], [9], [10], [11], [12], [13], [14], [15], [16], [17], [18], [19], [20], [21], a new solution that can be widely utilized and holds the generality is proposed in this article.

This article takes a 48–12 V three-phase regulated *LLC* converter with a resonant frequency of 1 MHz as the research object. In the input voltage range from 36 to 75 V, a new active current sharing scheme that can improve the gain range is discussed. Then, in order to achieve high-efficiency and high-power density, a novel multiphase resonant inductor and transformer structure is proposed. Finally, the magnetic elements are optimized by constructing the improved magnetic circuit model. The rest of this article is organized as follows. Section II introduces an inverse coupled resonant inductor (ICRI) design scheme, which can not only effectively expand the voltage gain range but also realize active current sharing of the converter. Section III discusses a comprehensive design scheme of high symmetric ICRI using PCB windings and integrated planar magnetics. Section IV describes the converter prototype and compares the proposed converter with the other state-of-the-art solutions.

## II. Proposed Comprehensive Current Sharing Scheme for Multiphase *LLC* Converter

### A. Three-Phase LLC Topology and Connection Scheme

The three-phase *LLC* converter with half-bridge structure can be divided into six kinds of topologies according to the connection mode. There are four connection modes at the primary side, which are Y-Primary, $\Delta$-Primary, $\Delta$-Cr network, and Y-Cr network, respectively. Meanwhile, there are two connection modes at the secondary side, which are Y-Secondary and $\Delta$-Secondary, respectively. In theory, the current sharing can always be achieved to a certain degree by adopting any kind of the above connection mode [25]. Then, the peak current and root-mean-square (RMS) current can be reduced by controlling the interleaving of phases. Furthermore, the conduction loss of the converter can be reduced. The above six connection modes can be freely combined to achieve better performance. Fei et al. [25], [26] systematically summarized the pros and cons of topologies adopting different connection modes. For the three-phase interleaved *LLC* converter, Y-connection mode and $\Delta$-connection mode are electrically equivalent to each other. Thus, this article considers Y-connection mode only to simplify the analysis.

Another advantage of the three-phase *LLC* is that it can easily integrate three inductors and three transformers into a single magnetic core, improve the power density, and maintain a small output current ripple [25], [26], [27].

When Y-connection mode is adopted in multiphase *LLC* converter, the resonant chamber has a common node. The converter, in which the common node is connected with the input ground, is called the system of neutral grounding. When the common node is floated, the resonant current of each phase needs to flow back through the resonant network of the other two phases [25], [26], [29].

For multiphase *LLC* converter, phase shading technology is usually used to improve efficiency at light load. However, for the three-phase magnetic integrated *LLC* converter with the floating node structure, due to the complex connection mode and inverse coupling effects of the resonant inductors of each phase, phase shading becomes complicated.

In order to exclude other coupling effects and independently analyze the influence of the inverse coupling between the resonant inductors on the converter, this article intends to adopt the simple parallel three-phase *LLC* topology proposed in [28], as shown in Fig. 1. The primary side of the topology adopts half-bridge structure, and the secondary side uses synchronous rectifier. For the convenience of expression, $i_{ri}$ and $i_i$ are defined as the RMS resonant current and the RMS out current of each phase, respectively, $i_{\mathrm{out}}$ as the total output current, and $V_{\mathrm{in}}$ and $V_{\mathrm{out}}$ as the input and output average voltages.

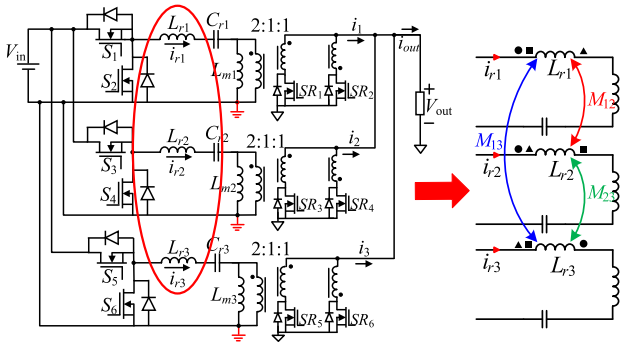


Fig. 1. Three-phase interleaved magnetic integration *LLC* converter.

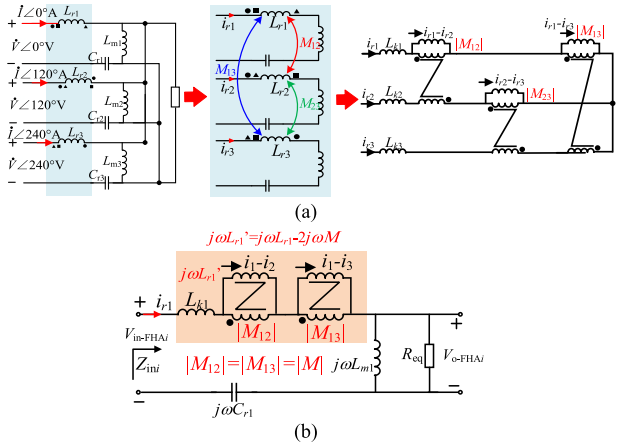


Fig. 2. AC equivalent circuit of resonant tank. (a) Three-phase converter. (b) One-phase converter.

### B. Effect of ICRIs on Gain

In this article, the resonant inductors of three-phase *LLC* converter adopt the inverse coupled inductor design, as shown in Fig. 1. In Fig. 1, $M_{ij}$ ($M_{ij}\leq 0$) represents the mutual inductance, and $-1/2\leq K_{ij}<0$ represents the coupling coefficient between phases. In order to simplify the analysis, it is assumed that the resonant inductance parameters of each phase are equal and the inverse coupling resonant inductor of each phase converter is coupled symmetrically. Therefore, we can get

$$\begin{cases} V_{\text{in}-1}=L_{r1}\cdot\frac{di_{r1}}{dt}+M_{12}\cdot\frac{di_{r2}}{dt}+M_{13}\cdot\frac{di_{r3}}{dt} \\ V_{\text{in}-2}=L_{r2}\cdot\frac{di_{r2}}{dt}+M_{12}\cdot\frac{di_{r1}}{dt}+M_{23}\cdot\frac{di_{r3}}{dt} \\ V_{\text{in}-3}=L_{r3}\cdot\frac{di_{r3}}{dt}+M_{23}\cdot\frac{di_{r2}}{dt}+M_{13}\cdot\frac{di_{r1}}{dt} \\ V_{\text{in}-1}=V_{\text{in}-2}=V_{\text{in}-3}=V_{\text{in}} \\ L_{r1}=L_{r2}=L_{r3}=L_r \\ M_{12}=M_{13}=M_{23}=M_{ij}=M \\ K_{ij}=K \\ M=K\sqrt{L_{ri}L_{rj}}=KL_r. \end{cases} \tag{1}$$

Since the converter still follows the basic working principle of the traditional *LLC*, the fundamental harmonic approximation (FHA) method can be used to analyze the circuit. The ac equivalent circuit of three-phase *LLC* converter with ICRIs is shown in Fig. 2(a). Assuming that the three-phase resonant inductors are symmetrically coupled, $M_{12}=M_{13}=M_{23}$, then, one-phase converter can be taken as an example for analysis; Fig. 2(b) shows the ac equivalent circuit of one-phase *LLC* converter. $V_{\text{in-FHA}\,i}$ represents the fundamental wave effective value of the input voltage of the phase resonant network, and $V_{\text{o-FHA}\,i}$ represents the fundamental wave effective value of the output voltage. We have

$$\begin{cases} V_{\text{in}-\text{FHA}}=\frac{2\sqrt{2}}{\pi}V_{\text{in}} \\ V_{o-\text{FHA}}=\frac{2\sqrt{2}}{\pi}V_{\text{out}} \\ \dot{I}_{r1}+\dot{I}_{r2}+\dot{I}_{r3}=0 \end{cases}. \tag{2}$$

Ignoring the leakage inductance of the transformer, the equivalent resonant inductance of each phase in Fig. 1 is $L'_{ri}=L_r-2M=(1-2K)L_r$. Then, we can get where $R_{\text{eq}}$ represents the ac equivalent impedance of one-phase converter, $R_{Li}$ represents the load resistor of one-phase converter, and $N$ represents the turn ratio of the transformer. By combining (2) and (3) shown at the bottom of the this page, it can be obtained

$$\begin{cases} \dot{V}_{\text{in}-\text{FHA1}}=\dot{I}_{r1}Z_1-Z_M(\dot{I}_{r2}+\dot{I}_{r3})=\dot{I}_{r1}(Z_1+Z_M) \\ \dot{V}_{\text{in}-\text{FHA2}}=\dot{I}_{r2}Z_2-Z_M(\dot{I}_{r1}+\dot{I}_{r3})=\dot{I}_{r2}(Z_2+Z_M) \\ \dot{V}_{\text{in}-\text{FHA3}}=\dot{I}_{r3}Z_3-Z_M(\dot{I}_{r1}+\dot{I}_{r2})=\dot{I}_{r3}(Z_3+Z_M) \end{cases}. \tag{4}$$

By analyzing (2)–(4), it can be seen that in the above vector operation, voltage vector and current vector influence the equivalent impedance of the converter. So, we cannot directly take the impedance $Z_i+Z_M$ in (4) as the equivalent impedance that actually participates in operation of the proposed converter, for two reasons.

$$\begin{cases} \dot{V}_{\text{in}-\text{FHA1}}=\dot{I}_{r1}\,(j\omega L_{r1}+1/j\omega C_{r1}+j\omega L_{m1}//R_{\text{eq}})-\dot{I}_{r2}j\omega M-\dot{I}_{r3}j\omega M \\ \dot{V}_{\text{in}-\text{FHA2}}=\dot{I}_{r2}\,(j\omega L_{r2}+1/j\omega C_{r2}+j\omega L_{m2}//R_{\text{eq}})-\dot{I}_{r1}j\omega M-\dot{I}_{r3}j\omega M \\ \dot{V}_{\text{in}-\text{FHA3}}=\dot{I}_{r3}\,(j\omega L_{r3}+1/j\omega C_{r3}+j\omega L_{m3}//R_{\text{eq}})-\dot{I}_{r1}j\omega M-\dot{I}_{r2}j\omega M \\ Z_1=j\omega L_{r1}+1/j\omega C_{r1}+j\omega L_{m1}//R_{\text{eq}} \\ Z_2=j\omega L_{r2}+1/j\omega C_{r2}+j\omega L_{m2}//R_{\text{eq}} \\ Z_3=j\omega L_{r3}+1/j\omega C_{r3}+j\omega L_{m3}//R_{\text{eq}} \\ Z_M=j\omega M \\ R_{\text{eq}}=8N^2R_{Li}/\pi^2 \end{cases} \tag{3}$$

First, we can see from the articles presented in [32], [33], [36], and [40] that when inverse coupled inductors are adopted in multiphase interleaved dc–dc converters, the equivalent inductance that actually participate in operation of the proposed converter needs to be calculated due to the mutual influence of each phase inductor. However, the value of such equivalent inductance is closely related to the voltage of the inductors and the duty cycle $D$. Moreover, the value of the equivalent inductance is different in each different operating mode. Due to the periodic variation of the equivalent inductance, Wang et al. [32], [33], [36], and [40] finally derive the equivalent steady-state inductance and equivalent transient inductance that actually affect the circuit operation by solving the equivalent inductance of each operating mode, respectively, and then adopting the equivalent decoupling method.

Second, in order to study the influence of the equivalent impedance of the highly symmetric multiphase inverse coupled inductors on the ac voltage gain of the proposed converter, we must figure out the effective ac impedance that actually participate in operation of the converter. However, this article adopts FHA to establish the ac equivalence model; the equivalent model only considers the fundamental voltage, which cannot accurately establish a high-precision equivalent impedance model for each operating mode in one switching period. In addition, the vector operation, as shown in (2)–(4), the value, and direction of the ac voltage and current are periodically changing over time. So, in the analysis of FHA, to accurately describe the effect and impact of ac voltage and current, a concept similar to average or valid values should be used to derive the ac impedance model equivalently. Only, in this way, we can obtain the effective ac impedance that actually participates in operation of the proposed converter.

In this article, it is assumed that symmetry and consistency are achieved between three-phase coupled inductors. Then, according to (1), the amplitude and effective value of each phase current are equal, which has $i_{r1} = i_{r2} = i_{r3}$. Based on this, the vector in (3)–(4) is operated on the modulus value, that is, the modulus of voltage vector and current vector is equivalent to the equivalent effective value of one switching period. Then, each phase converter has

$$\begin{cases} \left|\dot{V}_{\text{in-FHA1}}\right| = \left|\dot{V}_{\text{in-FHA2}}\right| = \left|\dot{V}_{\text{in-FHA3}}\right| = \left|\dot{V}_{\text{in-FHA}}\right| \\ \left|\dot{I}_{r1}\right| = \left|\dot{I}_{r2}\right| = \left|\dot{I}_{r2}\right| = \left|\dot{I}_{r}\right| \\ Z_1 = Z_2 = Z_3 = Z_r = j\omega L_r + 1/j\omega C_r + j\omega L_m//R_{\text{eq}} \end{cases}. \tag{5}$$

By adopting the modulus values of each voltage vector $|\dot{V}_{\text{in-FHA}}|$ and current vector $|\dot{I}_r|$ in (5) to replace the expressions of voltage vector and current vector in (3), the equivalent input impedance $Z'_{\text{in}i}$ of each phase converter under the action of inverse coupled inductor can be obtained as follows:

$$\begin{cases} Z'_{\text{in1}} = \dfrac{\left|\dot{V}_{\text{in-FHA1}}\right|}{\left|\dot{I}_{r1}\right|} = \dfrac{\left|\dot{I}_{r1}\right|Z_1 - Z_M\left(\left|\dot{I}_{r2}\right| + \left|\dot{I}_{r3}\right|\right)}{\left|\dot{I}_{r1}\right|} = Z_1 - 2Z_M \\ Z'_{\text{in2}} = \dfrac{\left|\dot{V}_{\text{in-FHA2}}\right|}{\left|\dot{I}_{r2}\right|} = \dfrac{\left|\dot{I}_{r2}\right|Z_1 - Z_M\left(\left|\dot{I}_{r1}\right| + \left|\dot{I}_{r3}\right|\right)}{\left|\dot{I}_{r2}\right|} = Z_2 - 2Z_M \\ Z'_{\text{in3}} = \dfrac{\left|\dot{V}_{\text{in-FHA3}}\right|}{\left|\dot{I}_{r3}\right|} = \dfrac{\left|\dot{I}_{r3}\right|Z_1 - Z_M\left(\left|\dot{I}_{r2}\right| + \left|\dot{I}_{r1}\right|\right)}{\left|\dot{I}_{r3}\right|} = Z_3 - 2Z_M \end{cases}. \tag{6}$$

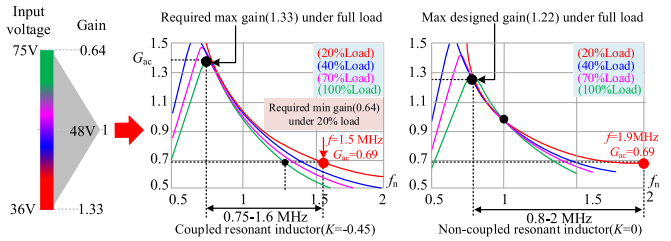


Fig. 3. Voltage gain curve of *LLC* converter under inverse ICRI and noncoupled resonant inductor.

Since the resonant inductors of each phase are symmetrically coupled, the input and output voltage parameters of three-phase converter are consistent. Thus, there is almost no difference in the operation of the resonant network of the three-phase converter. This study takes the single-phase converter for example and obtains the ac voltage gain $G_{\text{ac}}$ with ICRI as follows:

$$G_{\text{ac}} = \frac{V_{o-\text{FHA1}}}{V_{\text{in-FHA1}}} = \frac{j\omega L_{m1}//R_{\text{eq}}}{j\omega L_{r1} + 1/j\omega C_{r1} + j\omega L_{m1}//R_{\text{eq}} - 2j\omega M} = \frac{1}{\sqrt{\left[1+\frac{1}{h}(1-2K) - \frac{1}{f_n^2}\right]^2 + \left[Q(f_n(1-2K) - \frac{1}{f_n})\right]^2}}. \tag{7}$$

Furthermore, the ac voltage gain of the $n$-phase converter can be obtained as follows:

$$G_{\text{ac-n}} = \frac{V_{\text{o-FHA}}}{V_{\text{in-FHA}}} = \frac{j\omega L_m//R_{\text{eq}}}{j\omega L_r + 1/j\omega C_{r1} + j\omega L_m//R_{\text{eq}} - (n-1)j\omega M} = \frac{1}{\sqrt{\left[1+\frac{1}{h}(1-(n-1)K) - \frac{1}{f_n^2}\right]^2 + \left[Q(f_n(1-(n-1)K) - \frac{1}{f_n})\right]^2}} \tag{8}$$

where $h = L_m/L_r$ represents the inductance ratio, $n$ represents the number of working phases of the converter, $f_n = f_s/f_r$ represents the normalized frequency, $f_r$ represents the resonant frequency, and $Q = \sqrt{L_r/C_r}/R_{\text{eq}}$ represents the quality factor. It is known that quality factor $Q$ and inductance ratio $h$ have an important effect on the performance of the converter, especially the ac gain. Therefore, under the premise of realizing zero voltage switching (ZVS), the maximum voltage gain of large current should be maximized. In this way, the requirements of voltage regulation can be met within a small frequency range [30]. In this article, the input voltage range is 36–75 V, the output voltage is 12 V, the resonant frequency $f_r = 1$ MHz, the rated load current of per phase is 30 A, and the turns ratio is $n = 2$. Under these parameters, the ac voltage gain $G_{\text{ac}}$ should be within a range of at least 0.64–1.33. The design criterion of inductance ratio $h$ aiming to reduce loss is studied in [31]. Based on that, the appropriate value of $h = 4$ is determined in this article.

In order to show the advantages of the proposed solution and to select the proper design point, according to the above determined parameters and (6), the ac voltage gain characteristics of *LLC* converter with ICRI and noncoupled resonant inductor at each point with load variation have been simulated [30], and the results are shown in Fig. 3. From comparison, it can be observed that the inverse coupling of resonant inductor steepens the voltage gain curve and significantly increases the maximum

TABLE I
AC VOLTAGE GAIN AND COMPARISONS OF TWO *LLC* CONVERTER SOLUTIONS UNDER DIFFERENT LOADS AND OPERATING FREQUENCIES

| Operating Frequency $f$ (MHz) | AC voltage gain at 40% rated load | | | AC voltage gain at 70% rated load | | | AC voltage gain at rated load | | |
|---|---|---|---|---|---|---|---|---|---|
| | Proposed solution $G_{ac}$ | Traditional LLC $G_{ac\text{-}t}$ | Improvement of gain $\lvert G_{ac}\text{-}G_{ac\text{-}t}\rvert/G_{ac\text{-}t}$ | Proposed solution $G_{ac}$ | Traditional LLC $G_{ac\text{-}t}$ | Improvement of gain $\lvert G_{ac}\text{-}G_{ac\text{-}t}\rvert/G_{ac\text{-}t}$ | Proposed solution $G_{ac}$ | Traditional LLC $G_{ac\text{-}t}$ | Improvement of gain $\lvert G_{ac}\text{-}G_{ac\text{-}t}\rvert/G_{ac\text{-}t}$ |
| 0.5 | 1.04 | 0.98 | 6% | 0.85 | 0.77 | 10% | 0.71 | 0.65 | 9% |
| 1 | 1.02 | 1 | 2% | 0.98 | 1 | 2% | 0.97 | 1 | 3% |
| 1.2 | 0.79 | 0.83 | 5% | 0.76 | 0.82 | 7% | 0.72 | 0.79 | 9% |
| 1.5 | 0.62 | 0.69 | 10% | 0.59 | 0.65 | 9% | 0.54 | 0.61 | 11% |

voltage gain. Obviously, with different current design points, the desired maximum gain $G_{\max} = 1.33$ and minimum gain $G_{\min} = 0.64$ can be achieved when using ICRI. When noncoupled resonant inductors are adopted, the maximum voltage gain at full load and half load cannot reach 1.33. Besides, the maximum voltage gain can only be achieved by reducing the inductance ratio $h$, which will lead to an increase in transmission loss [30]. In addition, noncoupled resonant inductor will result in a very wide operating frequency range. Especially under light load (output current less than 20% rated load current), in order to achieve the voltage gain $G_{\min} = 0.69$, the operating frequency is as high as 2 MHz, which will lead to extremely low light-load efficiency. When ICRI is used, the frequency modulation range is from 0.75 to 1.45 MHz during the main operating conditions, and the maximum operating frequency is only 1.6 MHz under light load.

In order to further highlight the improvement of the proposed method on the gain of the converter, the gain curve in Fig. 3 is analyzed quantitatively. Beyond that, the percentage of the improvement in gain range by using ICRI is quantified in Table I. According to the quantitative comparison results in Table I, we can clearly know the ac voltage gain of the converter with and without coupled inductors in different frequencies and load currents. Then, the appropriate frequency regulation range can be selected according to the design requirements and other parameters. The above method is a general criterion for multiphase magnetically integrated *LLC* converter when designing with the requirement of the wide range.

In summary, when ICRI is adopted, frequency change exerts a more significant effect on the output voltage regulation. Therefore, with the change of load, the output voltage can be stabilized by slightly adjusting the switching frequency. While achieving high efficient operation with a wide input voltage range, it is beneficial to the design and optimal operation of magnetic elements.

### C. *Influence of Three-Phase ICRI on Current Sharing*

The performance of *LLC* converter is very sensitive to resonance parameters. When the resonance parameter error is merely 5%, the imbalance of load currents between phases can reach to more than 50% [24].

The equivalent circuit of one phase for three-phase *LLC* converter can be drawn, as shown in Fig. 4. According to the FHA analysis method, $V_{\text{in-FHA}i}$ represents the fundamental wave effective value of the input voltage modulated by the switch, $V_{Ri}$ represents the sum of the voltage of the resonant inductor and

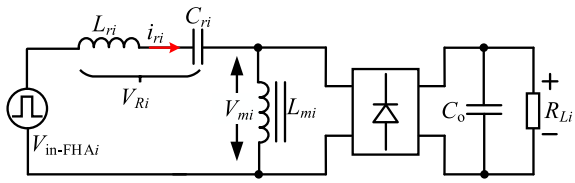


Fig. 4. Equivalent circuit of one-phase *LLC* converter.

the resonant capacitor, $V_{mi}$ represents the terminal voltage of the transformer, and $i_{ri}$ represents the resonant current of one phase. Taking the switching frequency as the fundamental frequency, the circuit variations in Fig. 4 are equivalent into corresponding parameters by using the FHA method. According to KVL law, the relationships can be given as follows:

$$\begin{cases} \dot{V}_{\text{in-FHA}i} = \dot{V}_{Ri} + \dot{V}_{mi} \\ \dot{V}_{Ri} = \dot{I}_{ri} j X_{ri} \\ \dot{V}_{mi} = \dot{I}_{ri} / \left( \frac{1}{X_{mi}} + \frac{1}{R_{Li}} \right) \end{cases} \tag{9}$$

where $X_{ri}$ and $X_{mi}$ refer to the reactance of the resonant chamber and excitation inductor branch, respectively, which are related to the working frequency and values of resonant inductors and capacitors. Then, the calculation formula can be expressed as follows:

$$\begin{cases} X_{ri} = \omega L_{ri} - \frac{1}{\omega C_{ri}} \\ X_{mi} = \omega L_{mi}. \end{cases} \tag{10}$$

According to the article presented in [29], the impedance of the resonant chamber will change with the working frequency. Under the same resonant parameters, when the working frequency is closer to the resonant frequency, the proportion of $X_{ri}$ changing with the change of the resonant frequency will increase. From (9) and (10), it can be observed that when the FHA method is used for analysis, the influence of the deviation of resonant inductors and resonant capacitors on $X_{ri}$ is equivalent. Next, the current distribution characteristics of the three-phase currents under different switching frequencies are analyzed.

As for the three-phase interleaved *LLC* converter, the current of each phase flows into the common node, and the sum of their instantaneous values is 0, then

$$\dot{I}_{r1} + \dot{I}_{r2} + \dot{I}_{r3} = 0 \tag{11}$$

where the input voltage of the resonant chamber of each phase is 120° different from each other, which will affect the current of each phase. The following equation can be obtained from (11)

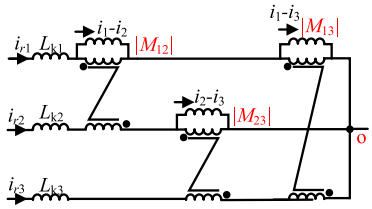


Fig. 5. Equivalent circuit model of the three-phase ICRI.

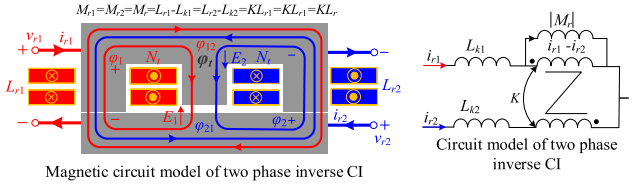


Fig. 6. Two-phase coupled inductor and its equivalent magnetic circuit model.

and (9)

$$\begin{aligned}&\left(\dot{V}_{m1}+\dot{I}_{r1}jX_1-V_{\text{in-FHA1}}\right)\\&+\left(\dot{V}_{m2}+\dot{I}_{r2}jX_2-V_{\text{in-FHA2}}\right)\\&+\left(\dot{V}_{m3}+\dot{I}_{r3}jX_3-V_{\text{in-FHA3}}\right)=0.\end{aligned}\tag{12}$$

Obviously, three-phase currents can form a triangle connected end-to-end in the vector diagram. One-phase current can be calculated according to the law of cosines

$$\left|\dot{I}_{r1}\right|^2=\left|\dot{I}_{r2}\right|^2+\left|\dot{I}_{r3}\right|^2-2\left|\dot{I}_{r2}\right|\left|\dot{I}_{r3}\right|\cos\left[\pi-\angle\left(\dot{I}_{r1},\dot{I}_{r2}\right)\right].\tag{13}$$

The relationship between three-phase currents can be obtained as follows:

$$\left(\left|\dot{I}_{r2}\right|-\left|\dot{I}_{r3}\right|\right)^2<\left|\dot{I}_{r1}\right|^2<\left(\left|\dot{I}_{r2}\right|+\left|\dot{I}_{r3}\right|\right)^2.\tag{14}$$

It can be observed that in the traditional three-phase *LLC* converter, the current distribution of each phase is strongly related to the actual resonant chamber reactance and excitation inductance of each phase. Besides, the essential problem that causes the unbalance current in the multiphase converter is mainly the inconsistency of the impedance of each phase or the mismatch of the impedance of each phase and the equivalent input voltage of the resonant network. From this perspective, influence mechanisms of errors of resonant inductors, resonant capacitors, and the excitation inductor on the current unbalance are the same, and their influence effects are equivalent.

Fig. 5 shows an equivalent circuit model of the proposed three-phase ICRI. When the phase parameters have errors, for example, when the equivalent input impedance satisfies $Z'_{\text{in1}} = Z'_{\text{in2}} \neq Z'_{\text{in3}}$, we have $i_{r1} = i_{r2} \neq i_{r3}$. If the difference of resonant current $|i_{r1}\text{-}i_{r3}|$ and $|i_{r21}\text{-}i_{r3}|$ changes, the magnetic flux $\varphi_m$ will be induced in the magnetic circuit. According to Lenz's law, the change trend and direction of $\varphi_m$ are opposite to the magnetic flux $\varphi_3$ corresponding to $i_{r3}$ and always hinder the change of $\varphi_3$. According to the law of electromagnetic induction, $\varphi_m$ will generate induced electromotive forces $E_1$ and $E_2$ in the first- and second-phase resonant inductors. Assuming that $i_{r1} = i_{r2} < i_{r3}$ at a certain moment, $i_{r1}$ and $i_{r2}$ will continue to increase under the influence of reverse electromotive forces $E_1$ and $E_2$, while $i_{r3}$ will continue to decrease, *and finally achieve steady-state uniform flow* $i_{r1} = i_{r2} = i_{r3}$.

Next, taking two phases for example, how the inverse coupling between resonant inductors affects the current distribution is analyzed quantitatively. Setting $\Delta i$ as the difference of resonant current and $\varphi_t$ as the total magnetic flux in the parallel coupled inductor, then the equation can be given as follows:

$$\Delta i = i_{r1} + i_{r2} = \frac{R_t \varphi_t}{N_t}.\tag{15}$$

According to (15) and the magnetic flux in Fig. 6 [6], it can be observed that the deviation of the input current $\Delta i$ is inversely proportional to the number of turns $N_t$ of the coupled inductor and is proportional to the total reluctance $R_t$. Besides, $\Delta i$ can be suppressed by increasing the inductance so as to achieve the current sharing.

According to the ac equivalent circuit model of the coupled inductor, the resonant can be given as follows:

$$\begin{cases}V_{\text{in-FHA1}}-V_{o-\text{FHA}}=i_{r1}j\omega L_{r1}+i_{r2}j\omega M+i_{r1}j\omega L_{r1}\\\quad -i_{r1}\frac{j}{\omega C_{r1}}\\V_{\text{in-FHA2}}-V_{o-\text{FHA}}=i_{r2}j\omega L_{r2}+i_{r1}j\omega M+i_{r2}j\omega L_{r2}\\\quad -i_{r2}\frac{j}{\omega C_{r2}}\end{cases}.\tag{16}$$

Since the two phases are phase shifted by 180°, the equation can be given as follows:

$$V_{\text{in-FHA1}}-V_{o-\text{FHA}}+V_{\text{in-FHA2}}-V_{o-\text{FHA}}=0.\tag{17}$$

According to equations above, we can get the following:

$$\frac{i_{r1}}{-i_{r2}}=\frac{L_{r2}+M+L_{r2}-\frac{1}{\omega^2 C_{r2}}}{L_{r1}+M+L_{r1}-\frac{1}{\omega^2 C_{r1}}}.\tag{18}$$

Due to the fact that the coupled inductors have different equivalent inductance and inductor expressions in each mode of a switching period [32], [33], it is difficult to express the relationship between the inductance of ICRI and the unbalance current in algebraic form directly. Therefore, the numerical calculation is used to discuss the law of the unbalance current under specific error parameters. Next, assuming that $Z'_{\text{in1}} = 0.9\,Z'_{\text{in2}}$, we have $i_{r1} > i_{r2}$. If the error of the two-phase currents is within 1%, the equation can be given as follows:

$$0.99 \leq \frac{i_{r1}}{-i_{r2}} \leq 1.01.\tag{19}$$

According to (18) and (19), the parameters of ICRI required to meet the design goal can be obtained. In order to simplify the analysis quantitatively, the maximum error rate of the resonance parameters $Z_{\text{error}}$ is defined as follows:

$$Z_{\text{error}}=\frac{\max\left[Z_{\text{in}i}-Z_{\text{in}j}\right]}{\sum_{i=1}^{3}Z_{\text{in}i}\Big/3}\tag{20}$$

where $\max[Z_{\text{in}i}\text{-}Z_{\text{in}j}]$ represents the maximum difference of input impedances between phases. The maximum unsharing degree of the currents $\text{CS}_{\text{error}}$ between three phases is defined

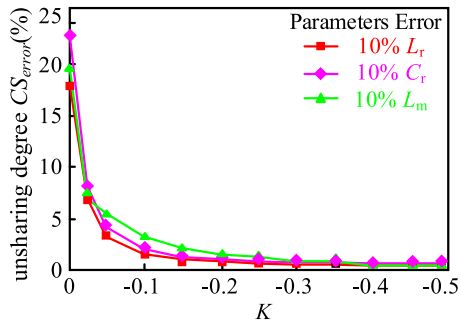


Fig. 7. Relationship between the coupling coefficient $K$ and current sharing.

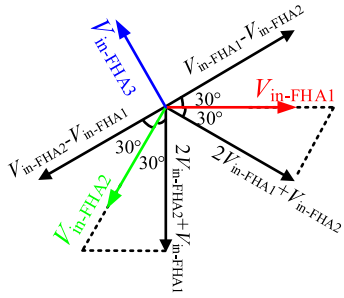


Fig. 8. Phase relationship of input voltage of three-phase *LLC* converter.

as follows:

$$\mathrm{CS_{error}} = \frac{\max\left[i_i - i_j\right]}{i_{\mathrm{out}}/3}. \tag{21}$$

Namely, if three-phase ICRI can meet the relationship in (1), through the above method, the quantitative influence of the change of the coupling coefficient of ICRI on the current distribution can be calculated. The relationship between the coupling coefficient $K$ and current sharing is shown in Fig. 7. Through three different parameter errors, the current sharing design basis based on multiphase ICRI is given. Finally, according to the design parameters and the desired current sharing degree, combining with the curve in Fig. 7, the design parameters of multiphase ICRI can be quickly solved.

According to (12), the controllable component can be changed by adjusting the equivalent amplitude of $V_{\mathrm{in\text{-}FHA}\,i}$ or the phase difference between $V_{\mathrm{in\text{-}FHA}\,i}$, which is equivalent to changing the equivalent impedance of the converter. Hence, the equivalent impedance of each phase can match the equivalent input voltage of each phase and then the current sharing of each phase can be realized. Based on this, the main active current sharing strategies are frequency modulation or phase shifting to realize current sharing.

Through the analysis above, it can be observed that in the proposed current sharing scheme based on ICRI, the mutual influence between the magnetic fluxes of each phase changes the actual equivalent impedance participating in the work of the converter, which is equivalent to changing the phase difference between each phase through phase shifting. Meanwhile, this provides a new idea for the study of the current sharing. If the relationship between the ICRI and the phase-shift angle can be established, and the change of the impedance of the resonant inductor can be equivalent to the phase change, then the influence of the ICRI on the current sharing will be transformed into the influence of the phase change on the current sharing.

According to (3)–(5), the matrix expression of the relationship between $V_{\mathrm{in\text{-}FHA}\,i}$ and $i_{ri}$ can be given as follows:

$$\begin{bmatrix} \dot{V}_{\mathrm{in-FHA1}} \\ \dot{V}_{\mathrm{in-FHA2}} \\ \dot{V}_{\mathrm{in-FHA3}} \end{bmatrix} = \begin{bmatrix} Z_1 & -Z_M & -Z_M \\ -Z_M & Z_2 & -Z_M \\ -Z_M & -Z_M & Z_3 \end{bmatrix} \begin{bmatrix} \dot{I}_{r1} \\ \dot{I}_{r2} \\ \dot{I}_{r3} \end{bmatrix}. \tag{22}$$

Due to the coupling between three phases, coefficients of the matrix in (22) are not full rank. In fact, the ICRI has different equivalent inductance in each working mode. In order to simplify the calculation, the average value is used directly in this article. First, we take first and second phases for example and convert (22) into a matrix with full rank of coefficients. Then, the relationship between currents and the input voltage can be obtained by inverting the coefficient matrix. Finally, the ratio of first- and second-phase current can be obtained as follows:

$$\frac{\dot{I}_{r1}}{\dot{I}_{r2}} = \frac{Z_2\left(2\dot{V}_{\mathrm{in-FHA1}}+\dot{V}_{\mathrm{in-FHA2}}\right)+Z_1\left(\dot{V}_{\mathrm{in-FHA1}}+\dot{V}_{\mathrm{in-FHA2}}\right)-2Z_M}{Z_1\left(\dot{V}_{\mathrm{in-FHA1}}+2\dot{V}_{\mathrm{in-FHA2}}\right)+Z_2\left(\dot{V}_{\mathrm{in-FHA2}}+\dot{V}_{\mathrm{in-FHA1}}\right)-2Z_M}. \tag{23}$$

Since the phase difference between $V_{\mathrm{in\text{-}FHA}\,i}$ is 120°, the angle relationship after mutual calculation can be obtained according to Fig. 8

$$\frac{\dot{I}_{r1}}{\dot{I}_{r2}} = \frac{\sqrt{3}\dot{V}_{\mathrm{in-FHA1}}\left(Z_2\angle -30^\circ + Z_3\angle 30^\circ\right)}{\sqrt{3}\dot{V}_{\mathrm{in-FHA2}}\left(Z_1\angle 30^\circ + Z_3\angle -30^\circ\right)}. \tag{24}$$

In addition, according to (3) and (9), another expression of the ratio of first- and second-phase current can be obtained as follows:

$$\frac{\dot{I}_{r1}}{\dot{I}_{r2}} = \frac{\dot{V}_{m1}/\left(Z_1 - jX_{r1}\right) - 2Z_M}{\dot{V}_{m2}/\left(Z_2 - jX_{r2}\right) - 2Z_M}. \tag{25}$$

According to (23)–(25), the relationship between input amplitude, phase, and coupling inductance of ICRI can be obtained. In addition, the relationship between the equivalent resistors of three phases can be given as follows:

$$\frac{1}{R_{L1}} + \frac{1}{R_{L2}} + \frac{1}{R_{L3}} = \frac{1}{R_{\mathrm{eq}-t}} \tag{26}$$

where $R_{\mathrm{eq}\text{-}t}$ represents the ac equivalent impedance of three-phase converter. From the analysis above, it can be observed that the equivalent load resistor $R_{Li}(i = 1,2,3)$ of the three-phase converter will change due to the deviation of three-phase parameters, the coupling effect of ICRI, and the current working frequency. An optimized phase-shifting modulation strategy is proposed to achieve the current sharing in [29]. According to the relationship between phase-shifting angle and parameter error described in [29], taking one-phase converter as the reference phase, the additional phase-shifting angles of the second phase and third phase are set as $\alpha_1$ and $\alpha_2$. In order to analyze the variation of the amplitude and phase of the neutral point voltage, the expression of the three-phase input voltage can be given as follows [29]:

$$\left|\dot{V}_{\mathrm{in-FHA}}\right|\sin\left[\omega t\right] + \left|\dot{V}_{\mathrm{in-FHA}}\right|\sin\left[\omega t - \left(\frac{2}{3}\pi + \alpha_1\right)\right] + \left|\dot{V}_{\mathrm{in-FHA}}\right|\sin\left[\omega t - \left(\frac{4}{3}\pi + \alpha_2\right)\right] = 0. \tag{27}$$

The amplitude and phase can be given as follows:

$$\begin{cases} \left|\Delta\dot{V}_{\text{in-FHA}i}\right| = \left|\dot{V}_{mi}\right|\sqrt{A^2+B^2}, \angle\left(\Delta\dot{V}_{\text{in-FHA}i}\right) \\ \quad = \arccos\left(\frac{A}{\sqrt{A^2+B^2}}\right) \\ A = 1-2\cos x\cos\left(y-\frac{\pi}{3}\right),\ B = 2\sin x\cos\left(y-\frac{\pi}{3}\right) \\ x = \frac{\alpha_1+\alpha_2}{2},\quad y = \frac{\alpha_1-\alpha_2}{2}. \end{cases} \tag{28}$$

According to the active current sharing control [29] and (27) and (28), $x$ and $y$ are related to the phase-shift angle $\alpha_1$ and $\alpha_2$. When there are errors in the parameters of each phase, by establishing the relationship between input amplitude, $x$ and $y$, the corresponding phase-shift angle can be solved. Then, the phase can be converted into coupling coefficient of ICRI based on the corresponding relationship between coupling effect and equivalent impedance in (2)–(5). Finally, by designing ICRI reasonably, the current sharing effect can be same as that under the phase-shift control. The proposed current sharing method is more suitable for the digital control system of the multiphase *LLC* converter, and it neither needs to implement phase-shifting control nor requires an additional current sharing loop.

To sum up, the coupling effect of ICRI is equivalent to the impedance change, and then the impedance change is equivalent to the adjustment of the phase and amplitude. Therefore, through coupled inductors, the impedance can be changed to achieve the current sharing, which provides a new passive control strategy for studying the current sharing problem of the multiphase *LLC* converter. Due to the limited space, this article only theoretically analyzes the equivalent relationship between the coupling coefficient and the phase-shift control in order to prove the mathematical mechanism and basis of the proposed method, without, for example, analysis and parameter calculation. However, in order to verify that the proposed method has good current sharing effect in various resonant parameter errors, the following part investigates the relationship between the value of coupling coefficient $K$ and the effect of current sharing by using the comprehensive simulation method.

Simplis is used for simulation and the simulation parameters are $V_{\text{in}} = 48$ V, $V_{\text{out}} = 12$ V, and $i_{\text{out}} = 90$ A. Other simulation parameters are set by four groups as follows.

1) The first group of parameters: $L_{ri}$ and $L_{mi}$ of each phase are the same but $C_{ri}$ is different. In this way, the error of input impedance of each phase is mainly caused by $C_{ri}$. And we set $Z_{\text{in1}} = 0.9Z_{\text{in}}$, $Z_{\text{in2}} = Z_{\text{in}}$, and $Z_{\text{in3}} = 1.1Z_{\text{in}}$.
2) The second group of parameters: $C_{ri}$ and $L_{mi}$ of each phase are the same but $L_{ri}$ is different. In this way, the error of input impedance between each phase is mainly caused by $L_{ri}$. And we set $Z_{\text{in1}} = 0.9Z_{\text{in}}$, $Z_{\text{in2}} = Z_{\text{in}}$, and $Z_{\text{in3}} = 1.1Z_{\text{in}}$.
3) The third group of parameters: $L_{ri}$ and $C_{ri}$ of each phase are the same but $L_{mi}$ is different. In this way, the error of input impedance between each phase is mainly caused by $L_{mi}$. And we set $Z_{\text{in1}} = 0.9\ Z_{\text{in}}$, $Z_{\text{in2}} = Z_{\text{in}}$, and $Z_{\text{in3}} = 1.1Z_{\text{in}}$.
4) The fourth group of parameters: $L_{ri}$, $C_{ri}$, and $L_{mi}$ of each phase are different. And we set $Z_{\text{in1}} = 0.9Z_{\text{in}}$, $Z_{\text{in2}} = Z_{\text{in}}$, and $Z_{\text{in3}} = 1.1Z_{\text{in}}$.

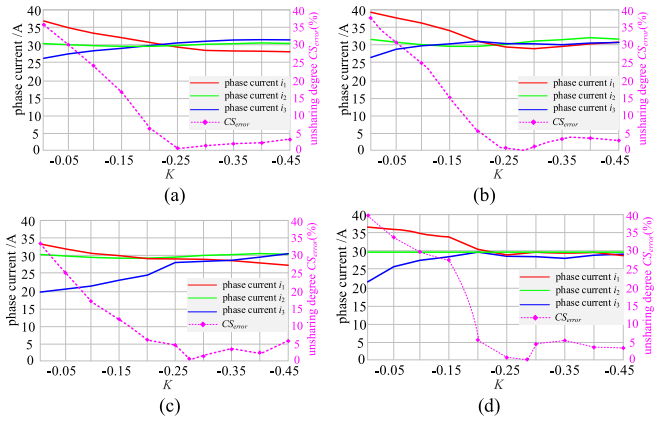


Fig. 9. Relationship between coupling coefficient and current sharing. (a) First group simulation result. (b) Second group simulation result. (c) Third group simulation result. (d) Fourth group simulation result.

From the simulation result in Fig. 9, it can be observed that under the four groups of parameters, inverse coupling can significantly improve the effect of current sharing. When the coupling coefficient $K = 0$, the maximum unsharing degree $\text{CS}_{\text{error}}$ is as high as 33%–40%. Meanwhile, with the increase of coupling strength, the $\text{CS}_{\text{error}}$ presents a trend of rapidly decreasing first and then slowly increasing. In the range of $-0.45 \le K \le -0.2$, the $\text{CS}_{\text{error}}$ of the four curves is all less than 5%, and the best current sharing effect is achieved when $-0.28 \le K \le -0.25$, at where $\text{CS}_{\text{error}}$ is approximately equal to 0.

By comparing and analyzing Figs. 7 and 9, it can be observed that there is a common conclusion according to the comprehensive simulation results and theoretical analysis. Namely, no matter what type of parameter error the three-phase converter is, when the proposed current sharing solution is adopted, the best current sharing effect can be achieved when $-0.28 \le K \le -0.25$, at where $\text{CS}_{\text{error}}$ is approximately equal to 0. The difference between the two is the range of $-0.45 \le K \le -0.3$.

From the theoretical analysis and the conclusion in Fig. 7, it can be observed that when the current sharing effect reaches the best in the range of $-0.28 \le K \le -0.25$, continuing to increase the coupling strength has no impact on the current sharing effect. According to the comprehensive simulation results, as shown in Fig. 9, when the best current sharing effect is achieved, the $\text{CS}_{\text{error}}$ presents a trend of slowly increasing, but the $\text{CS}_{\text{error}}$ of the four curves is all less than 5%. The main reason for the difference above is that the FHA method is adopted in the theoretical analysis, and the high-frequency harmonics are ignored. However, coupled inductors are adopted in this article, and the waveform of the resonant current will change slightly. In addition, the ICRI can be equivalent to different inductance parameters in each mode of a switching period of the converter, resulting in the equation being too complex, and it is difficult to express directly in algebraic form. However, the comprehensive simulation method, as shown in Fig. 9, makes up for this shortcoming, and the relationship between coupling coefficient and the current sharing can be displayed more accurately. Therefore, it is recommended to take $-0.28 \le K \le -0.25$ as the best design

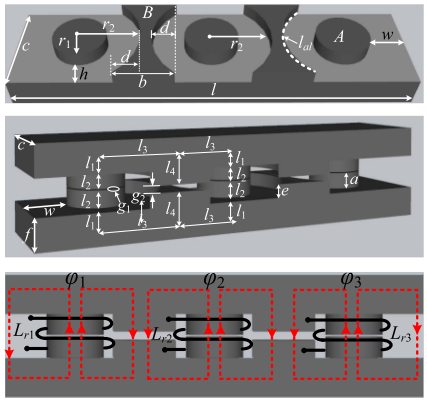


Fig. 10. Proposed ICRI.

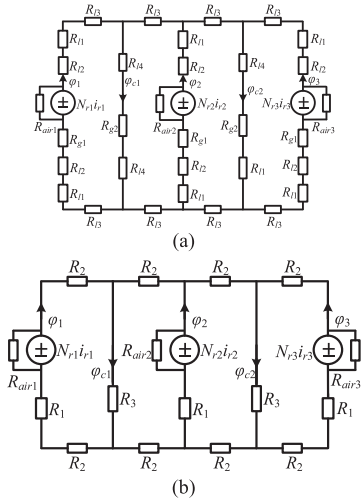


Fig. 11. Magnetic circuit model of the three-phase ICRI. (a) Basic model. (b) Equivalent simplified model.

area in the actual design. According to the analysis above, the coupling coefficient is also related to the gain of the converter. Therefore, in the design of the converter, the influence of the coupling coefficient on many aspects of the converter should be comprehensively considered to select the most appropriate design parameters.

Apart from improving the gain curve and suppressing the current unsharing, the inverse coupling of resonant inductors can also increase the input impedance and improve the transmission efficiency. However, this is not the focus of this article, which will not be discussed in detail.

## III. Comprehensive Design Scheme of Highly Symmetrical Three-Phase ICRI

### A. Proposed Three-Phase ICRI

Fig. 10 shows the three-phase ICRI proposed in this article. Its structure is similar to parallel EQ cores and has good coupling position. The central circular column A is chosen because it has the minimum winding loss for a given cross-sectional area [34]. The edges of the two core legs B in Fig. 10 are arc shaped to facilitate the design of PCB windings with larger cross-sectional area. In addition, the fringing flux or diffusion flux of air gap $g_1$ distribution around the main air gap has a radius of $a$. Besides, the regulating magnetic column B is designed as a circular arc so that the windings at the outermost edge can be kept away from the center of the air gap. Thus, the loss caused by diffusion magnetic flux around the air gap can be minimized [35].

The structure of parallel couple inductor (CI) has $L_{r1} = L_{r3} \neq L_{r2}$. The coupling coefficient can be adjusted by controlling the magnetic circuit length $l_i$ and the air gap length $g_i$ between the upper and lower magnetic cores. Then, the magnetizing inductance values of $L_{r1}$ and $L_{r3}$ can be greatly adjusted by the magnetic circuit $w$ at both ends of the magnetic core and the leakage flux of the air outside the winding. Finally, the consistency and high symmetry of the three-phase ICRI can be realized [36].

In order to obtain a high-precision magnetic circuit model, the edge effect of air gaps magnetic field and the leakage flux outside the windings are taken into consideration. As shown in Fig. 11(a), the magnetomotive force $N_{r1}i_{r1}$, $N_{r2}i_{r2}$, and $N_{r3}i_{r3}$ are paralleled with the air reluctance outside the winding $R_{\text{air1}}$, $R_{\text{air2}}$, and $R_{\text{air3}}$. Meanwhile, $R_{li}$ and $R_{gi}$ correspond to the reluctance of magnetic circuit length $l_i$ and the air gap $g_i$, respectively. Then, we can get

$$\begin{cases} R_{l1} = \frac{1}{\mu_0\mu_r} \cdot \frac{l_1}{c \cdot 2r_1},\ R_{l2} = \frac{1}{\mu_0\mu_r} \cdot \frac{l_2}{\pi r_1^2} \\ R_{l3} = \frac{1}{\mu_0\mu_r} \cdot \frac{l_3}{c \cdot f},\ R_{g1} = \frac{1}{\mu_0} \cdot \frac{g_1}{\pi r_1^2} \\ R_{l4} = \frac{1}{\mu_0\mu_r} \cdot \frac{l_4}{cb - 2 \cdot \left[\frac{l_{al}}{2\pi r_2} \cdot \pi r_2^2 - \frac{1}{2} c \cdot (r_2 - d)\right]} \\ \quad = \frac{1}{\mu_0\mu_r} \cdot \frac{l_4}{c(b + r_2 + d) - l_{al} r_2} \end{cases} \tag{29}$$

where $\mu_0$ represents the air permeability, $\mu_r$ represents the relative permeability, and $l_1 = f/2$, $l_2 = a$, $l_3 = r_2 + (b/2) - d$, and $l_4 = e + (f/2)$.

Considering the magnetic field edge effect of the main air gap $g_2$ [37], we can get

$$R_{g2} = \frac{1}{\mu_0 \left[\frac{b}{g_2} + \frac{2}{\pi}\left(1 + \text{In}\frac{\pi e}{2g_2}\right)\right] \cdot c}. \tag{30}$$

For the convenience of calculation, the magnetic circuit can be simplified to the equivalent model, as shown in Fig. 11(b). In the figure, $R_1 = 2R_{l1} + 2R_{l2} + R_{g1}$, $R_2 = R_{l3}$, and $R_3 = 2R_{l4} + R_{g2}$.

According to the modeling method of the air reluctance outside the winding proposed in [38], the air reluctance model outside the first-phase (third-phase) winding is obtained, as shown in Fig. 12. Obviously, the magnetic lines of force around the second-phase windings can be divided into two parts: the proximal part $R_{bi}$ and the distal part $R_{ai}$.

In this article, the magnetic resistance $R_{ai}$ of the distal part is divided into four identical quarter-spherical regions $R_{a1}$, two identical semicylindrical regions $R_{a2}$, and another semicylindrical region $R_{a3}$. And the magnetic resistance $R_{bi}$ of the proximal part is divided into two identical semicylindrical regions $R_{\text{b1}}$, two identical semicylindrical regions $R_{\text{b2}}$, and four identical quarter-spherical regions $R_{\text{b3}}$.

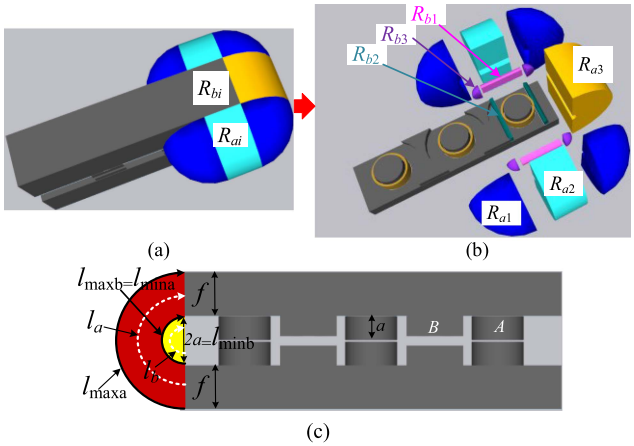


Fig. 12. Air magnetic field line model outside the windings of the first-phase (third-phase) inductor. (a) Magnetic resistance model. (b) Equivalent cutting model. (c) Section diagram and magnetic field line length.

Fig. 12(c) shows a profile of the air reluctance outside the winding. The red region corresponds to the reluctance $R_{ai}$ of the distal part, while the yellow region corresponds to the reluctance $R_{bi}$ of the proximal part. In the figure, $l_b$ and $l_a$ represent the average magnetic circuit length of reluctance $R_{bi}$ and reluctance $R_{ai}$, and we have $l_b = (l_{\max b}+l_{\min b})/2$, $l_a = (l_{\max a}+l_{\min a})/2$, $l_{\min b} = 2a$, $l_{\max b} = l_{\min a} = \pi a$, and $l_{\max a} = \pi(f+a)$. Thus, each reluctance can be gained as follows:

$$\begin{cases} R_{b1} = \frac{1}{\mu_0}\cdot\frac{l_b}{S_{b1}}, R_{b2} = \frac{1}{\mu_0}\cdot\frac{l_b}{S_{b2}}, R_{b3} = \frac{1}{\mu_0}\cdot\frac{l_b}{S_{b3}} \\ R_{a1} = \frac{1}{\mu_0}\cdot\frac{l_a}{S_{a1}}, R_{a2} = \frac{1}{\mu_0}\cdot\frac{l_a}{S_{a2}}, R_{a3} = \frac{1}{\mu_0}\cdot\frac{l_a}{S_{a3}} \\ S_{b1} = \frac{V_{b1}}{l_b} = \frac{\pi a^2 r_1}{l_b} = S_{b2},\ S_{b3} = \frac{V_{b3}}{l_b} = \frac{\pi a^3}{3l_b} \\ S_{a1} = \frac{V_{a1}}{l_a} = \frac{\pi f r_1\cdot(f+2a)}{l_a}, S_{a2} = \frac{V_{a2}}{l_a} = \frac{\pi\left[(h+a)^3-a^3\right]}{3l_a} \\ S_{a3} = \frac{V_{a3}}{l_a} = \frac{\pi c(f^2+2fa)}{2l_a} \end{cases} \tag{31}$$

where $S_{bi}$ and $S_{ai}$ refer to the average cross-sectional area of each corresponding area. $V_{bi}$ and $V_{ai}$ refer to the volumes of the corresponding region.

Similarly, the air reluctance model outside winding 2 can be obtained. The expression of air reluctance outside each winding $R_{\mathrm{air}i}$ is obtained [36] as follows:

$$\begin{cases} R_{\mathrm{air1}} = R_{\mathrm{air3}} = \frac{R_{b1}}{2}//\frac{R_{a1}}{2}//\frac{R_{b2}}{2}//R_f//\frac{R_{b3}}{4}//\frac{R_{a2}}{4} \\ R_{\mathrm{air2}} = \frac{R_{b1}}{2}//\frac{R_{a1}}{2}//\frac{R_{b2}}{2}//\frac{R_{b3}}{4}//\frac{R_{a2}}{4} \end{cases}. \tag{32}$$

In the following part, the first phase is taken as an example to calculate the equivalent inductance, and the equivalent reluctance of the first phase is shown in Fig. 13. We can get the following:

$$\begin{cases} R_{\mathrm{I}} = \frac{(R_1+2R_2)R_3}{R_1+2R_2+R_3} \\ R_{\mathrm{II}} = \frac{(R_{\mathrm{I}}+2R_2)R_1}{R_{\mathrm{I}}+2R_2+R_1} \\ R_{\mathrm{III}} = \frac{(R_{\mathrm{II}}+2R_2)R_3}{R_{\mathrm{II}}+2R_2+R_3} \end{cases}. \tag{33}$$

Eventually, the expressions of self-inductance $L_{ri}$ and leakage inductance $L_{ki}$ of ICRI of different phases are obtained as follows:

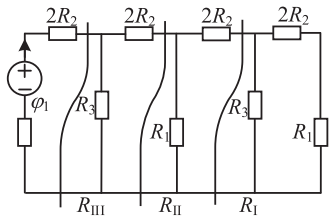


Fig. 13. Equivalent reluctance of the ICRI of the first phase.

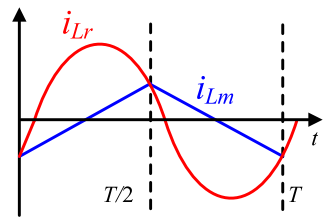


Fig. 14. Traditional simplified resonant network current model.

$$\begin{cases} L_{r1} = L_{r3} = \frac{N^2}{R_1+2R_2+R_{\mathrm{III}}} + \frac{N^2}{R_{\mathrm{air1}}} \\ L_{r2} = \frac{N^2(R_{\mathrm{I}}+R_{\mathrm{III}}+4R_2)}{(R_{\mathrm{I}}+2R_2)(R_{\mathrm{III}}+2R_2)+R_1(R_{\mathrm{I}}+R_{\mathrm{III}}+2R_2)} + \frac{N^2}{R_{\mathrm{air2}}} \\ L_{k1} = L_{k3} = \frac{N^2R_{\mathrm{III}}}{R_3(R_1+2R_2+R_{\mathrm{III}})}\cdot\left[1+\frac{R_1R_{\mathrm{II}}}{(R_{\mathrm{I}}+2R_2)(R_{\mathrm{II}}+2R_2)}\right] \\ \qquad + \frac{N^2}{R_{\mathrm{air1}}} \\ L_{k2} = \frac{N^2\left[(R_{\mathrm{III}}+2R_2)R_{\mathrm{I}}+(R_1+2R_2)R_{\mathrm{III}}+\frac{R_{\mathrm{I}}R_{\mathrm{II}}R_3}{R_{\mathrm{II}}+2R_2+R_3}\right]}{R_3(R_1+2R_2)(R_{\mathrm{III}}+2R_2)+R_1R_3(R_{\mathrm{I}}+R_{\mathrm{III}}+4R_2)} + \frac{N^2}{R_{\mathrm{air2}}} \end{cases} \tag{34}$$

### B. Calculation and Optimal Design of Three-Phase ICRI

Since all MOSFETs of the high-frequency *LLC* converter implement soft switching, the switching loss and drive loss of the proposed three-phase *LLC* converter are small. The main loss is the conduction loss and magnetics loss under high-frequency and high-current condition. Besides, the winding loss of magnetic components is much greater than the core loss so that the focus of loss analysis and efficiency optimization is the conduction loss of the winding. In this article, a higher precision conduction loss model of the proposed high-frequency *LLC* converter with ICRI is carried out. On this basis, the loss analysis and optimization design of the integrated three-phase ICRI are conducted.

In the construction of the transmission model of the resonant network, the resonant current and excitation current of the traditional *LLC* converter are defaulted to sinusoidal wave and triangular wave, respectively, as shown in Fig. 14. The expression of the effective value of the resonant current is obtained as follows:

$$I_r = \frac{\pi V_o}{2\sqrt{2}\cdot nR_{Li}}\sqrt{1+\frac{\pi^4}{64}\frac{1}{(hQ)^2}}. \tag{35}$$

Under the condition of high frequency and high current, the resonant current will inevitably produce large ac conduction loss.

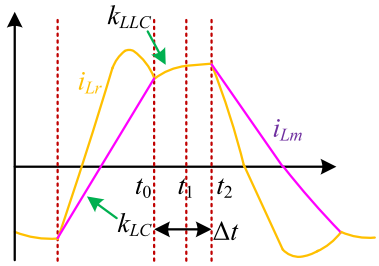


Fig. 15. High-precision resonant current model considering deadtime and inverse coupling.

In addition, the proposed three-phase *LLC* converter adopts the ICRI, as shown in Figs. 1 and 10. The inverse coupling will affect and change the current model of the resonant network, while the analysis and calculation of winding loss of magnetic components are closely related to the accurate resonant current model, which is directly associated with the optimal design of the integrated planar three-phase ICRI.

At present, the magnetic cores are suitable for the frequency of 1 MHz, and their permeability mostly decreases with the increase of temperature, which leads to the decline of the resonant inductor. Apart from that, the deadtime of high-frequency *LLC* converter accounts for a pretty big part of its duty period, which, thus, cannot be directly ignored. Based on this, the conduction loss model of *LLC* converter with ICRI is studied as follows.

*1) High-Precision Resonant Current Model of the Proposed LLC Converter With ICRI:* As shown in Fig. 27, a high-precision resonant current model that considers the effects of inverse coupling of resonant inductor, inductance parameter mismatch, and deadtime is constructed to better guide the loss analysis and optimal design.

If the initial time of $i_r(t) = i_m(t)$ is $t_0$, then we have $i_r(t_0) = i_m(t_0) = i_L(t_0)$. If the deadtime $t_d$ starts at $T_1$ and stops at $T_2$, we have $t_d = t_2 - t_1$ and $i_r(t_1) = i_m(t_1) = i_L(t_1)$.

When the working frequency $f$ is not equal to the resonant frequency $f_r$, the operating cycle $T \neq T_r$ and the rising slope of the magnetizing current under *LC* and *LLC* resonant modes are $K_{LC} = n_{DCX}\, V_{DCXo}/L_m$ and $K_{LLC} = V_{DCX\text{in}}/(L_m+L_r)$, and we have

$$\begin{cases} \frac{i_L(t_0)+i_L(t_1)}{T_r/2} = \frac{n\cdot V_o}{L_m} = K_{LC} \\ \frac{i_L(t_1)-i_L(t_0)}{(T-T_r-2t_d)/2} = \frac{V_{\text{in}}}{L_r+L_m} = K_{LLC} \end{cases}. \tag{36}$$

Based on (35), we can obtain

$$\begin{cases} i_L(t_0) = \frac{nV_oT_r}{4L_m} - \frac{V_{\text{in}}(T-T_r-2t_d)}{4(L_r+L_m)} \\ i_L(t_1) = \frac{nV_oT_r}{4L_m} + \frac{V_{\text{in}}(T-T_r-2t_d)}{4(L_r+L_m)} \end{cases}. \tag{37}$$

Since $L_{mi}$ is much larger than $L_{ri}$, we can consider the current $i_L(t_d)$ through them during deadtime to be constant, indicating that $i_L(t_d) = i_L(t_1) = i_L(t_2)$. According to the high-precision resonant current model in Fig. 15, when $T \neq T_r$, the secondary-side current $i_S(t)$ of the *LLC* converter is obtained as follows:

$$\begin{cases} i_S(t) = n\cdot I_{P-M}\sin(\omega_r t) & 0 \le t \le \frac{T_r}{2} \\ i_S(t) = n\cdot I_{P-M}\sin(\omega_r t) & \frac{T}{2} \le t \le \frac{T+T_r}{2} \end{cases} \tag{38}$$

where $I_{P\text{-}M}$ represents the maximum current of the primary side and can be presented as $I_{P\text{-}M} = \pi^* I_{ri}{}^* 0.5T^*n^*T_r$. In addition, $I_{ri}$ is the effective value of the primary-side current of *LLC* converter of each phase. To sum up, during a duty period, the resonant current at each stage can be expressed as follows:

$$i_{ri} = \begin{cases} K_{LC}\cdot t - i_L(t_1) + \frac{i_S(t)}{n}, & 0 \le t < \frac{T_r}{2} \\ K_{LLC}\cdot(t-\frac{T_r}{2}) + i_L(t_0), & \frac{T_r}{2} \le t < \frac{T}{2} - t_d \\ i_L(t_d) = i_L(t_1), & \frac{T}{2} - t_d \le t < T/2 \\ -K_{LC}(t-\frac{T}{2}) + i_L(t_1) - \frac{i_S(t)}{n}, & \frac{T}{2} \le t < \frac{T+T_r}{2} \\ -K_{LLC}(t-\frac{T+T_r}{2}) - i_L(t_0), & \frac{T+T_r}{2} \le t < T - t_d \\ i_L(t_d) = i_L(t_1), & T - t_d \le t < T \end{cases}. \tag{39}$$

According to Fig. 15 and formula (35)–(39), we can obtain the effective value expression of the improved high-precision resonant current where $I_{P\text{-}M}$ can be calculated from the equivalent impedance of the ICRI of the proposed *LLC* converter, as shown in Fig. 2 and (34). It can be observed that the improved resonant current model is related to resonant period $T_r$, switching cycle $T$, equivalent resonant inductor $L_r$', excitation inductance $L_m$, and deadtime $t_d$.

*2) Design Examples and Optimization Analysis:* Wu and Shi [31] studied the influence of deadtime $t_d$ and ratio $h$ between magnetizing inductor and resonant inductor on the conduction loss of *LLC* converter and summarized the relationship between parasitic parameters, such as input capacitance $C_{iss}$ and output capacitance $C_{oss}$ and deadtime selection when different types of MOSFET were used.

First, based on the design parameters, such as voltage and current, the selection of MOSFET and driver is determined, and parameters, such as $V_{\text{in}}$, $V_o$, $T$, $T_r$, and $I_r$ are known. Then, according to the optimal design criteria in [31], the deadtime $t_d$ = 50 ns and inductor ratio $h$ = 4 that should meet the efficiency optimization target can be calculated. Finally, based on the resonant current model in (40) shown at the bottom of the next page and design parameters of the proposed converter, the three-phase ICRI is designed, and loss analysis and volume optimization are carried out as follows.

In this article, the self-inductance of each phase ICRI $L_{ri}$ = 250 nH, the inductor ratio $h$ = 4, and the coupling coefficient $K$ = −0.4. Furthermore, the $L_{ki}$ of each phase in (34) is obtained. In addition, DMR51 magnetic core is adopted in this article. According to the data manual of magnetic core [39], the winding turns $N_r$ = 1, specific loss $P_v$ = 120 mW/cm$^3$, and $B_m$ = 165 mT are taken to obtain the cylindrical cross-sectional area $A_e$ and the cross-sectional area of the main air gap in Fig. 16. After that, the size parameters of magnetic cores, such as $r_1$, $r_2$, $b$, and $c$, can be obtained by combining (34) and the optimal efficiency design criterion [30], [31]. In order to avoid core saturation, the $w$ value should meet $w < c\text{-}r_1$.

Given the output current $i_{\text{out}}$ and current density $J$, the cross-sectional area of PCB winding $A_{\text{cu}} = i_{\text{out}}/3J$ can be obtained. Beyond that, the area of the magnetic core window $A_w$ should be slightly larger than 5%–10% of the cross-sectional area of

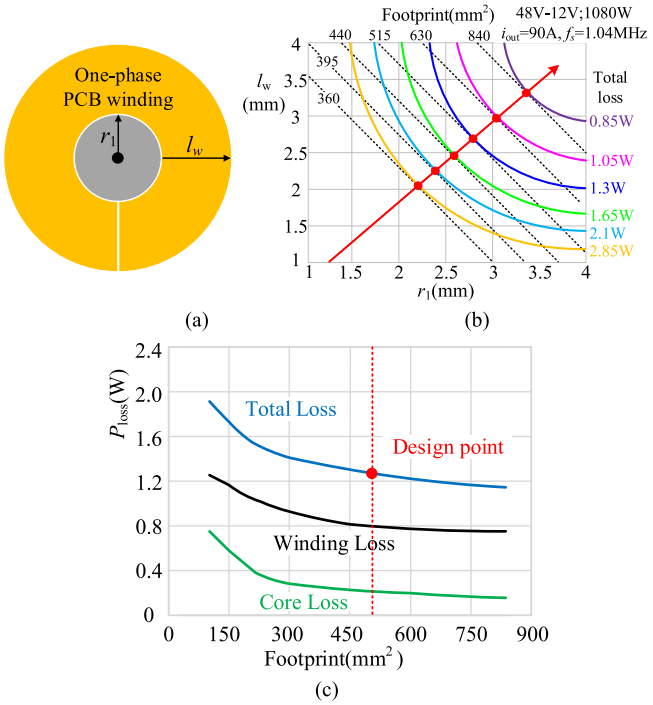


Fig. 16. Optimal design of ICRI. (a) Schematic of one-phase PCB winding and magnetic core. (b) Total loss and footprint versus core radius $r_1$ and winding width $l_w$ for the proposed ICRI. (c) Optimal ICRI footprint versus loss.

TABLE II
FOOTPRINT OF THE INTEGRATED THREE-PHASE ICRI

| Dimension parameters | Value (mm) | Dimension parameters | Value (mm) |
|---|---|---|---|
| $l$ | 26 | $h$ | 0.8 |
| $c$ | 4 | $d$ | 1.4 |
| $f$ | 2.2 | $a$ | 2.4 |
| $b$ | 3.2 | $e$ | 1.8 |
| $w$ | 2.8 | $g_1$ | 1 |
| $l_{a1}$ | 6.5 | $g_2$ | 2.2 |
| $r_1$ | 1.2 | $r_2$ | 2.6 |

TABLE III
PARAMETERS OF THREE-PHASE ICRI

| Parameters of the proposed ICRI | Value |
|---|---|
| Self-Inductances (nH) $L_{r1}$, $L_{r2}$, $L_{r3}$, $L_{r4}$ | 250, 250, 250 |
| Leakage inductances (nH) $L_{k1}$, $L_{k2}$, $L_{k3}$, $L_{k4}$ | 150, 150, 150 |
| Magnetizing Inductances (nH) $L_{m1}$, $L_{m2}$, $L_{m3}$, $L_{m4}$ | 100, 100, 100 |
| Volume (mm$^3$) | 1000 |
| Resistance of PCB winding (mΩ) | 1.2 |

the winding $A_{cu}$. Based on this, the values of $h$ and $d$ in Fig. 16 can be obtained. Then, through (29)–(34), the air gap lengths $g_1$ and $g_2$ and magnetic circuit lengths $f$ and $a$ can be obtained, and $e = (2a+g_1-g_2)/2$.

In summary, the basic design parameters of the magnetic core and winding can be obtained. Due to the fact that the number of turns $N_r = 1$ and the primary-side current is small, the winding design is relatively simple. In the loss analysis, it is found that the core losses are dominating. During the design, the main difficulty is to achieve the optimal balance between the efficiency and the power density of ICRI.

The proposed ICRI takes the thickness of PCB winding as 4 oz. Fig. 16(a) shows the schematic of one-phase PCB winding and magnetic core. In Fig. 16(a), $l_w$ and $r_1$ are the main factors affecting the volume and loss of the CI. Based on the loss model of parallel multiphase coupled inductors with planar integrated cores [40], [41] and the resonant current model in (40), we take the core radius $r_1$ and the winding width $l_w$ as the $x$-axis and $y$-axis, as shown in Fig. 16(b), which is the designed ICRIs total loss $P_{loss}$ contour and footprint contour with the different $l_w r_1$ values. In Fig. 16(b), the tangential points between the total loss and given footprint are the optimal design points. In this article, we set the footprint = 515 mm$^2$ in Fig. 16(b) as the optimal design points between the total loss and given footprint. Besides, ICRIs core loss and winding loss and total loss with the corresponding optimal footprint are calculated and shown in Fig. 16(c). It can be observed from the change trend of the total loss curve in Fig. 16(c) that before the slope slows down, the total loss of the resonant CI can be greatly reduced by increasing the volume. Thus, the red dashed in Fig. 16(c) is the optimal design that shows a good tradeoff between loss and volume for the proposed ICRI.

Finally, according to the inductance formula (34), current formula (40), and the design value in Fig. 16, the optimal design parameters of footprint of the proposed three-phase ICRI can be obtained, as shown in Table II. According to the proposed magnetic circuit model, inductance parameters and resistance value of the ICRI meeting the design requirements in this article can be obtained, as shown in Table III.

*3) Optimized Design Flow and Optimized Design Criteria:* To sum up, the optimization design flow and design criteria of the three-phase interleaved magnetically integrated *LLC* converter and ICRI proposed in this article can be summarized.

First, the parameter design goal of *LLC* converter is to ensure the soft switching, realize the requirements of the converter gain, and minimize the conduction loss of the converter. The design flow of *LLC* converter is shown in Fig. 17 [40].

Second, this article presents the parameter optimization design criteria of the designed three-phase ICRI considering volume and efficiency, including the parameter optimization design of the integrated planar magnetic core and PCB windings. The design flow is as follows.

$$I_r = \sqrt{\frac{1}{T}\left\{\begin{array}{l} T_r\left[\frac{I_{P-M}}{2}+\frac{K_{LC}^2T_r^2}{12}-\frac{K_{LC}^2 i_L(t_1)T_r}{2}+i_L^2(t_1)+\frac{I_{P-M}(K_{LC}T_r-4i_L(t_1))}{\pi}\right] \\ +(T-T_r-2t_d)\left[\frac{K_{LLC}^2}{3}\left(\frac{T-T_r}{2}-t_d\right)^2+K_{LLC}i_L(t_0)\left(\frac{T-T_r}{2}-t_d\right)+i_L^2(t_0)\right]+2t_d i_L^2(t_d) \end{array}\right\}} \quad (40)$$

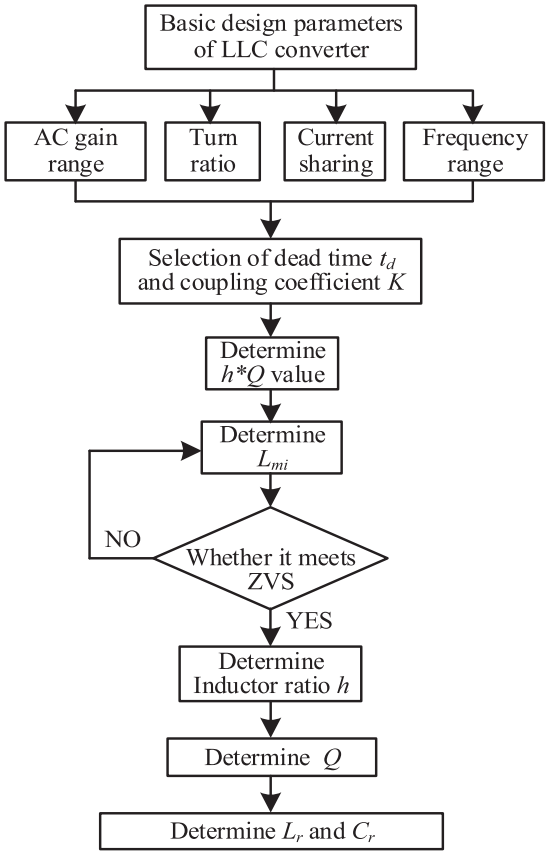


Fig. 17. Design flowchart of *LLC* converter parameters [40].

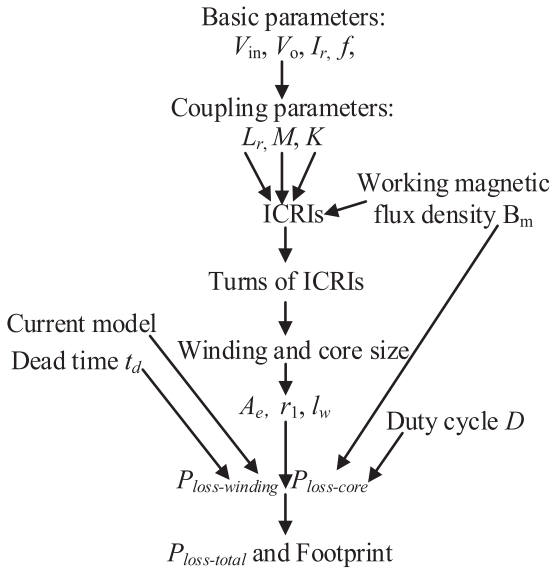


Fig. 18. Design flowchart for the proposed three-phase ICRI.

TABLE IV
PARAMETERS OF DESIGNED ICRI

| Inductance (nH) | Self-Inductance $L_{r1}$, $L_{r2}$, $L_{r3}$ | Leakage-Inductance $L_{k1}$, $L_{k2}$, $L_{k3}$ | Volume ($mm^3$) |
|---|---|---|---|
| Design value | 250, 250, 250 | 150, 150, 150 | 1000 |
| Simulation value | 244, 250, 245 | 149, 151, 150 | 1190 |
| Measurement value | 245, 251, 247 | 148, 150, 149 | 1195 |

1) First, based on the parameters of the proposed three-phase *LLC* converter and the design flowchart of the *LLC* converter, as shown in Fig. 17, the selection of MOSFET, the inductance ratio $h$, coupling coefficient $K$, switching frequency $f$, optimal deadtime $t_d$, and the parameters of resonant elements $L_r$ and $C_r$ can be determined in turn.
2) Second, according to the core structure in Fig. 10 and the winding arrangement in Fig. 16, the number of turns of ICRI can be determined first. Then, the volume and size parameters of the magnetic core that can meet the inductance value and coupling coefficient can be calculated based on (34).
3) Finally, according to the efficiency optimization method and loss model of the parallel multiphase coupled inductor proposed in [40], combining with the resonant current model in [40], the coupled inductor loss can be related to size parameters. Furthermore, the footprint of the integrated planar core and PCB windings can be optimized, including length, width, and height of the magnetic core, and the cross-sectional area $A_e$ of the core, inner diameter, outer diameter, and thickness of PCB windings. The loss of proposed ICRI is briefly summarized in Fig. 18.

### C. Maxwell Finite-Element Simulation of Three-Phase ICRI

First, the ANSYS Maxwell software and *LCR* are used to simulate and measure the self-inductance and mutual inductance values of the designed ICRI. Moreover, the results are shown in Table IV. Obviously, the measured data, the simulation results of finite-element software, and the theoretical design inductance value are highly consistent, and the error of the three is less than 4%. It proves that the magnetic circuit model established in this article has the high accuracy. Besides, the new magnetic circuit model is characterized by universality and expansibility. Thus, it can be applied to the analysis and design of parallel multiphase CIs with similar structures.

Then, Maxwell three-dimensional (3-D) finite-element software is used for simulation. Beyond that, we put 120% rated resonant current into each phase's winding and simulate magnetic core legs' peak flux densities of each phase at maximum operating frequency $f_{\max} = 1.6$ MHz. The results are shown in Fig. 19. It can be observed that the magnetic cores of each phase are not saturated, which proves the rationality of the design in this article.

Finally, in the Maxwell 2-D simulation environment, the magnetic flux distribution of each phase is simulated and shown in Fig. 20. The result indicates that the magnetic flux mainly includes the main flux through cylinder A and the mean gap $g_1$ in Fig. 16, the leakage flux in the main air gap $g_2$ and core leg B, and the bypass flux formed by the air magnetic field lines outside the winding. Among them, the main flux stores most of the magnetic field energy. Beyond that, the majority of the main flux only passes through the cylinder A and the small gap $g_1$, and only a small part passes through the atmospheric gap $g_2$. The

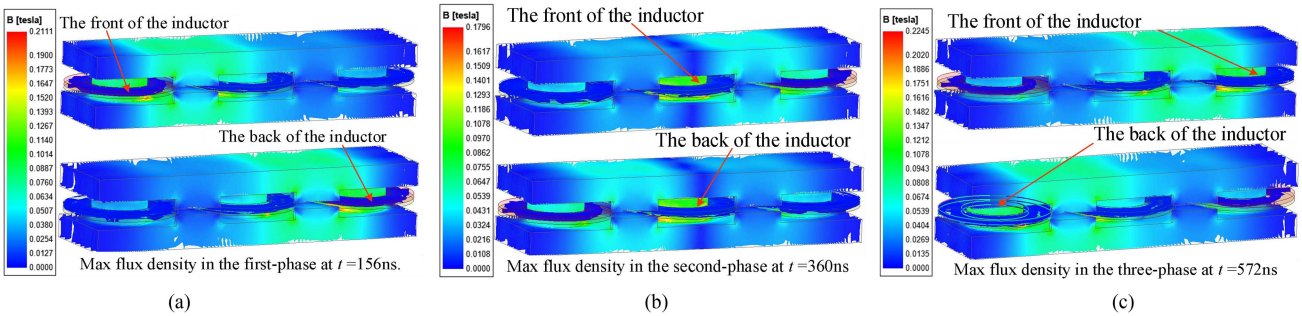


Fig. 19. Maxwell finite-element simulation of flux density for the proposed ICRI.

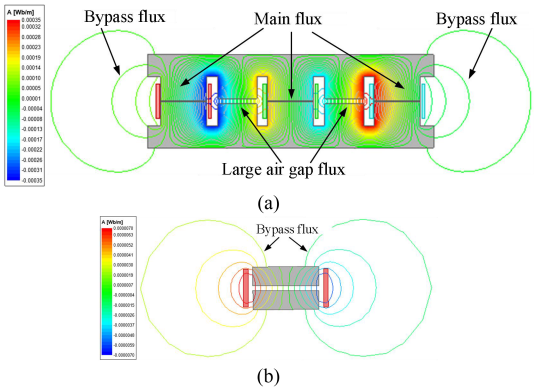


Fig. 20. Simulation of flux distribution for the proposed ICRI.

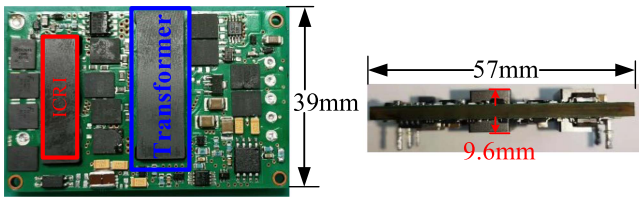


Fig. 21. Designed converter prototype.

TABLE V
PARAMETERS OF DESIGNED *LLC* CONVERTER PROTOTYPE

| Parameter | Value |
|---|---|
| Input voltage range $V_{in}$ | 36–75 V |
| Regulated output voltage $V_{out}$ | 12 V |
| Max output power | 1080 W |
| $L_r$ | 250 nH |
| $C_r$ | 100 nF |
| $L_m$ | 1000 nH |
| Operating frequency | 0.75–1.6 M |
| Primary devices | FDMD85100 |
| Secondary devices | BSZ010NE2LS5 |
| Magnetic materials | DMR51 |
| Footprint (L * W * H ) | 57 mm*39 mm*9.6 mm |

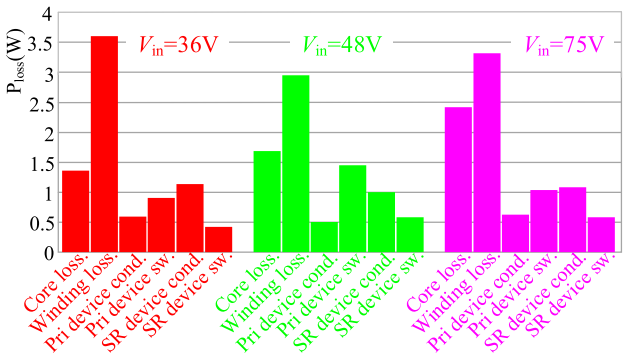


Fig. 22. Total converter devices' loss breakdown at different conditions ($i$ = 30 A).

leakage flux and bypass flux both pass through the atmospheric gap $g_2$. Since the magnetic flux passing through it is very small, the induced eddy current is also small.

## IV. Converter Prototype Design and Experimental Analysis

### A. Converter Prototype Design

The magnetic core structure and magnetic circuit model presented in this article can not only extend the number of phases but also be applied to the design of the three-phase magnetic integrated transformers. In this article, the core objective of magnetic element optimization is to balance power density and efficiency. Besides, the specific design methods and steps are the same as the above three-phase resonant inductor, which will not be described.

The designed converter prototype is shown in Fig. 21. Converter's output power is 1080 W (12 V, 90 A) at about a quarter of the brick volume, and the power density is 716 W/in$^3$. The converter can meet the voltage regulation requirements during all operating conditions in the frequency range of 0.75–1.6 MHz, and the main design parameters are given in Table V. Due to the current sharing, one phase can be used as an example, its total devices' loss breakdown under different input voltage is shown in Fig. 22, and the winding loss and core loss in Fig. 22 include ICRI and integrated transformer.

### B. Experimental Results of the Converter Prototype

Due to the use of PCB winding and integrated magnetic components, the resonant current test system is realized by a

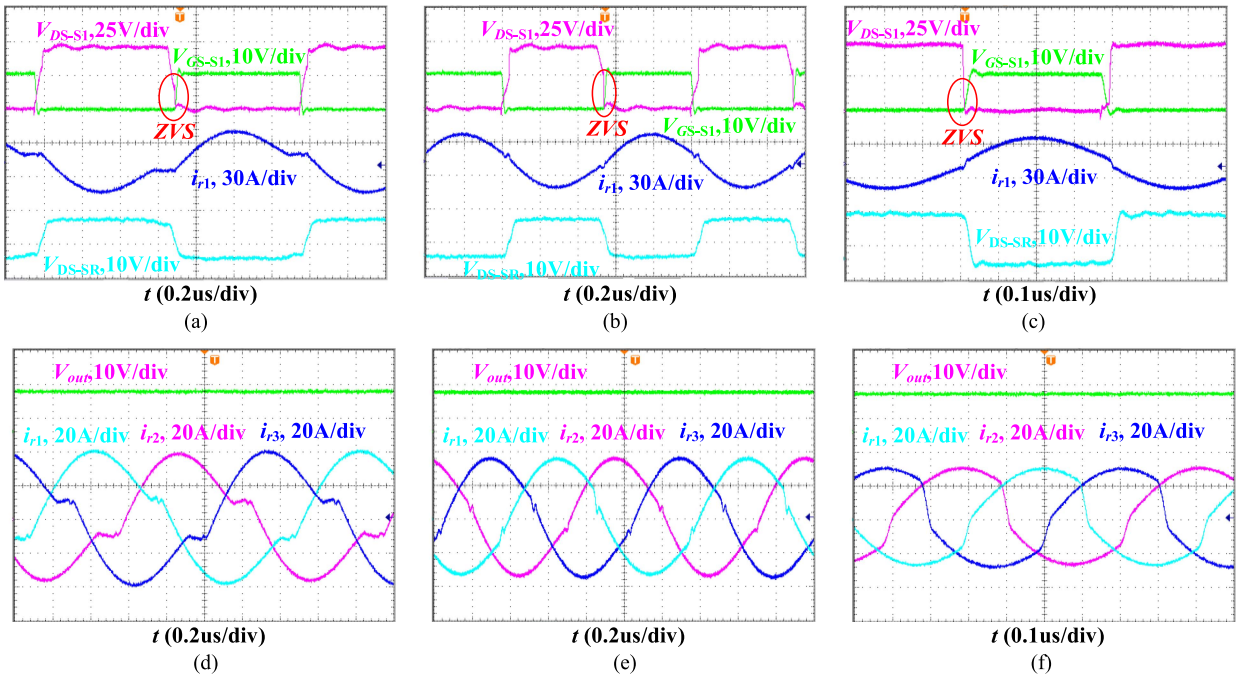


Fig. 23. Steady-state experimental waveforms. (a) Primary-side device $V_{gs}$ and $V_{ds}$ voltages, secondary-side $V_{ds}$ voltage and resonant current of the first phase when $V_{\text{in}} = 48$ V. (b) $V_{\text{in}} = 36$ V. (c) $V_{\text{in}} = 75$ V. (d) Resonant current when $V_{\text{in}} = 36$ V and $Z_{\text{error}}\% = 15\%$. (e) Resonant current when $V_{\text{in}} = 48$ V and $Z_{\text{error}}\% = 15\%$. (e) Resonant current when $V_{\text{in}} = 75$ V and $Z_{\text{error}}\% = 15\%$.

closed-loop Hall sensor CHB-25NP with a turn ratio of $N = 1/1000$ and a resistance of $R_m = 1000\ \Omega$, and the current is displayed through an oscilloscope.

Taking the first phase as an example, the steady-state test waveforms at $V_{\text{in}} = 48$ V, 36 V, and 75 V under rated current $i_{\text{out}} = 90$ A are shown in Fig. 23. It can be observed that under all three input voltages, the devices on the original and secondary sides can realize soft switching operation. Then, the resonant current of each phase is tested by changing the resonant element of the prototype to make the maximum error rate of each phase resonant parameter $Z_{\text{error}} = 15\%$. Meanwhile, the result is shown in Fig. 23(d)–(f). It can be observed that the current sharing scheme proposed in this article can achieve good current sharing performance when $V_{\text{in}} = 48$ V, 36 V, and 75 V.

The thermal image of the main elements at different input voltages is shown in Fig. 24. It can be observed that when $V_{\text{in}} = 75$ V, the maximum temperature of the converter is 102 °C for the ICRI and 105 °C for the magnetic integrated transformer. This is mainly because the magnetic circuits and windings of the integrated magnetic parts are relatively concentrated, which is also the main shortcoming of parallel integrated magnetic elements. Therefore, it is necessary to pay attention during design and try not to form local hotspots. In addition, the temperatures of MOSFETs of all phases are almost equal, which indirectly verifies good current sharing.

Fig. 25 shows the efficiency curves of the converter at different input voltages. It can be seen that the efficiency of the converter is the highest when it works near the resonant frequency $f_r$; otherwise, the efficiency will decrease. But within the input

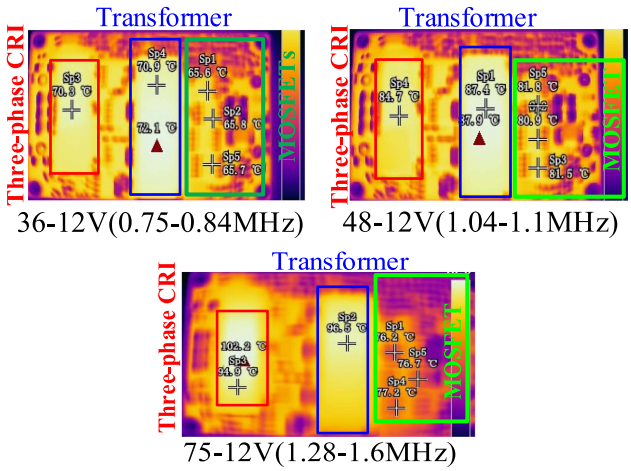


Fig. 24. Converter full-load thermal image at different input voltages.

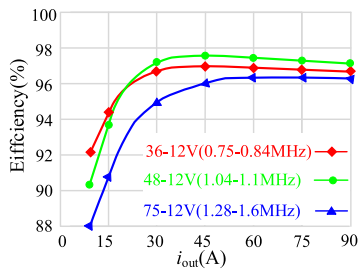


Fig. 25. Efficiencies of converter at different input voltages.

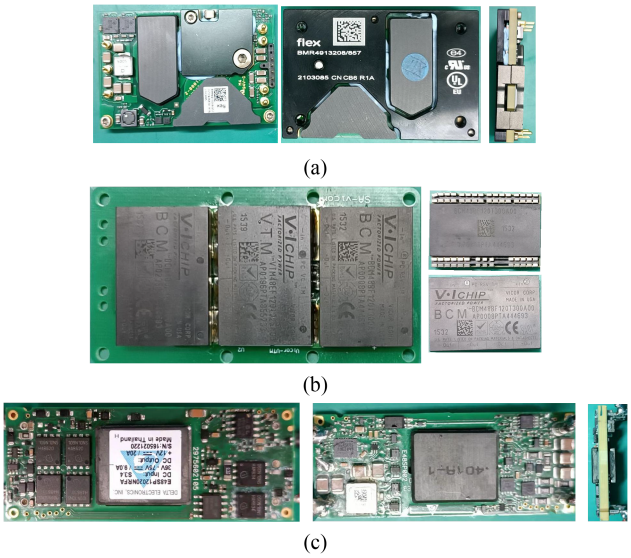


Fig. 26. Commercial power modules. (a) BMR4913208/857 of Flex Power. (b) DCM3623T75H13C2T of Vicor. (c) E48SK12038NRDH of Delta.

TABLE VI
PARAMETERS OF CONVERTER PROTOTYPES

| Parameter | BMR-4913208/857 of Flex [42] | DCM-3623T75H13C2T of Vicor [43] | E48SK-12038NRDH of Delta [44] |
|---|---|---|---|
| Input voltage | 48–60 V | 36–75 V | 36–75 V |
| Output voltage | 12 V | 12 V | 12 V |
| Output power | 1540 W | 320 W | 450 W |
| Frequency | 0.17–0.19 MHz | 0.3–1 MHz | 0.25 MHz |
| Footprint | 1/4 brick | 3623 Chip | 1/8 brick |

voltage range designed in this article, the maximum efficiency is kept above 96%, and the overall efficiency of the converter is kept above 94% under all conditions.

### *C. Comparison Between the Proposed Converter and Other State-of-the-Art Solutions*

In order to further explain the performance of the proposed converter, the comprehensive performance of the converter designed in this article is compared with other state-of-the-art solutions [30] and 12 V regulated isolated module power products [42], [43], [44]. To be specific, the comparison is made from five aspects, which are output ripple and noise, transient response, load transient voltage deviation, full-load thermal image, and comprehensive efficiency (max efficiency and full-load efficiency).

Fig. 26 and Table VI present the three groups of experimental comparison prototypes and their main parameters. Among them, intermediate bus converter BMR4913208/857 of Flex Power Company [42] uses Flex Power's leading patented technology and hybrid regulated ratio (HRR) topology. It can deliver 12 V/1540 W continuous power, making it the highest power density one-fourth brick digital dc/dc isolated power module for 48-V bus converter available on the market. Commercial power module DCM3623T75H13C2T from Vicor Power Company [43] adopts Vicor's leading patented technology, which is the sinusoidal amplitude converter (SAC) topology and the patented converter housed in package (CHIP) technology, making it the highest power density digital dc/dc isolated power module with wide input voltage available on the market.

In order to improve power density and efficiency, the commercial power module does not integrate electromagnetic interference (EMI) filter internally. However, commercial products need to comply with safety EMI and other standards. Therefore, output filters with the same parameters are configured for each group of experimental prototypes in this article.

In addition, in Fig. 26, the output power of each commercial power module is different. In order to perform the comparative experiment under the same load condition, backboard is designed in this article to parallel multiple commercial power modules to increase the output power. And the volume of backboard and filter is not included in the calculation of the power density of each converter.

Finally, in order to compare the performance of each converter fairly, integrated heatsink of commercial power module is also removed in this article. And the thermal test platform of commercial power modules adopts exactly the same heat dissipation conditions as the proposed converter in this article.

1) First, under the same experimental conditions and rated voltage (48 V/12 V), the steady-state and dynamic characteristics of the proposed converter and commercial power modules are tested, respectively. In this article, the power resistor is used as the output load, and load step 45 A-90 A-45 A is conducted on the four groups of converters, respectively. The experimental waveform is shown in Fig. 27.

It is obvious that the load current step-up time $\Delta t_{\rm up}$ (load step 45 A–90 A) of the proposed converter is 4 $\mu$s. Namely, when the load current step is changed from half load to full load, the current transient response speed of the proposed converter is 11 A/$\mu$s, and the load transient voltage deviation is 85 mV. When the load current changes from full load to half load (load step 90 A–45 A), the converter transient response speed of the proposed converter and load transient voltage overshoot are 9 A/$\mu$s and 130 mV, respectively. At the rated voltage and full-load current, the output ripple and noise of the proposed converter is 40 mV.

In order to facilitate comparative analysis, Table VII compares the experimental results of four groups of prototypes. It can be observed that the proposed converter adopts multiphase interleaved magnetic integration technology, which not only reduces the total output ripple and noise but also has higher switching frequency and bandwidth. Therefore, the proposed converter has the best steady-state and transient performance compared with the three groups of commercial power modules.

2) Next, under the same experimental conditions, the thermal image comparison of four converter prototypes at nominal condition (48/12 V) with same load current of 90 A is shown in Fig. 28. Analysis shows that, first of all, when the four experimental prototypes are working at the same voltage and current, the thermal image of commercial power module DCM3623T75H13C2T from Vicor has the

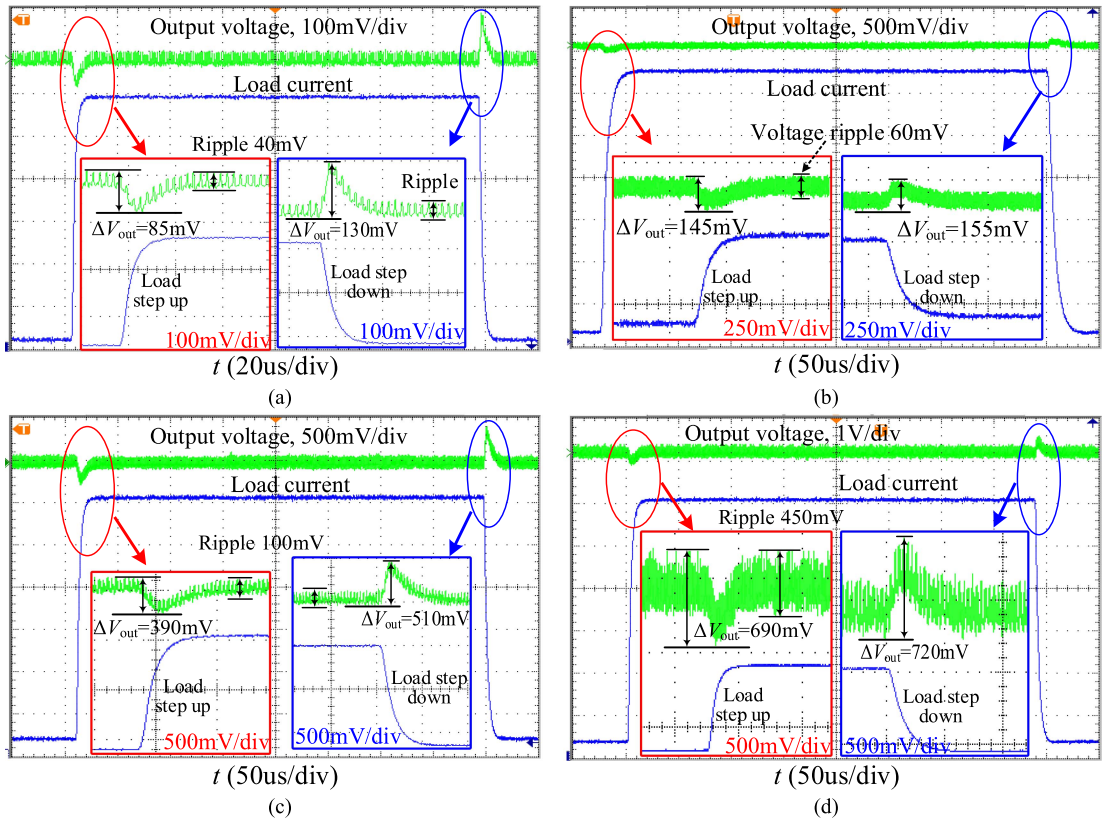


Fig. 27. Transient response, output ripple, and noise when load step 45 A-90 A-45 A. (a) Proposed converter. (b) Commercial power module BMR4913208/857. (c) Commercial power module DCM3623T75H13C2T. (d) Commercial power module E48SK12038NRDH.

TABLE VII
STEADY-STATE AND TRANSIENT EXPERIMENT OF CONVERTERS

| Parameter | Proposed converter | BMR4913208/857 of Flex [42] | DCM3623T75H13C2T of Vicor [43] | E48SK12038NRDH of Delta [44] |
|---|---|---|---|---|
| Transient response ( load step 45 A–90 A) | 11 A/$\mu$s | 5 A/$\mu$s | 4.5 A/$\mu$s | 6.5 A/$\mu$s |
| Transient response (load step 90 A–45 A) | 9 A/$\mu$s | 4.5 A/$\mu$s | 4 A/$\mu$s | 5.5 A/$\mu$s |
| Load transient voltage deviation (load step 45 A–90 A) | 85 mV | 145 mV | 390 mV | 690 mV |
| Load transient voltage deviation (load step 90 A–45 A) | 130 mV | 155 mV | 510 mV | 720 mV |
| Output ripple and noise | 40 mV | 60 mV | 100 mV | 450 mV |

lowest temperature. This is mainly due to the adoption of the Vicor's patented CHIP technology. Therefore, the highest temperature of the converter is only 65 °C.

Second, the proposed converter and other three commercial power modules all adopt the design scheme of the integration of magnetic components with embedded windings in the PCB. Thus, it can be seen that the highest temperature of the integrated magnetic components is greater than 95 °C under an ambient temperature of 25 °C and a fan speed of 100 Linear ft/min (LFM). And because the switching frequency of BMR4913208/857 and E48SK12038NRDH is only 0.18 MHz and 0.25 MHz, so under the same condition, the maximum temperature of MOSFETs is slightly lower than that of the proposed converter.

Finally, because the proposed converter adopts the multiphase integrated coupled inductor and transformer structure, the windings and magnetic cores are more compact and the magnetic flux is more concentrated compared with commercial power modules. Hence, the highest temperature (87.9 °C) occurs at the integrated coupled inductor of the proposed converter. Nonetheless, there is still a large margin for the temperature rise.

3) The measured efficiency of four converter prototypes under different load currents is shown in Fig. 29. As the input voltage range and maximum output power of each converter are different, the commercial power modules and the proposed converter are separately tested and compared according to the parameter characteristics of each converter.

Through analysis of Fig. 29(a), it can be observed that when the input voltage are 48 V and 54 V, respectively, the efficiency curves of the proposed converter and commercial power module BMR4913208/857 are basically the same. However, with the increase of input voltage, the proposed converter can achieve

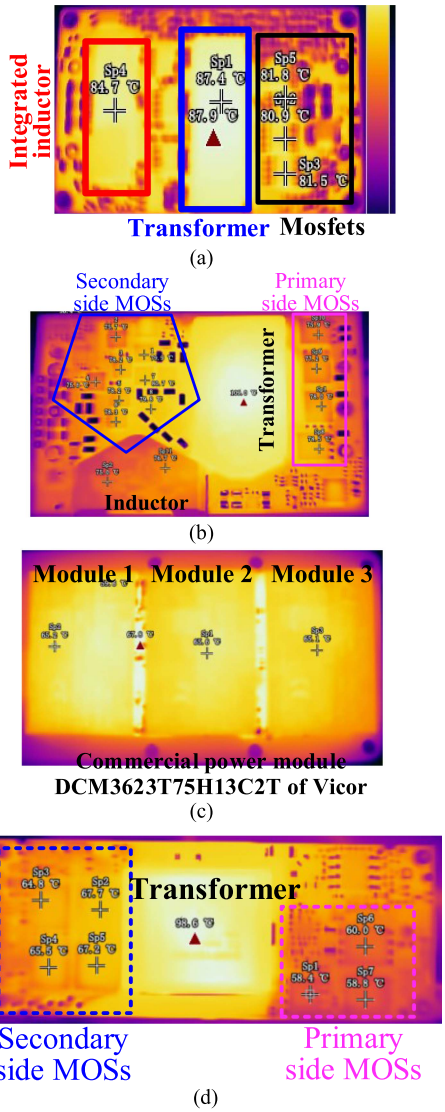


Fig. 28. Thermal test when 48–12 V and load current 90 A under an ambient temperature of 25 °C and a fan speed of 100 LFM. (a) Proposed converter. (b) Commercial power module BMR4913208/857. (c) Commercial power module DCM3623T75H13C2T. (d) Commercial power module E48SK12038NRDH.

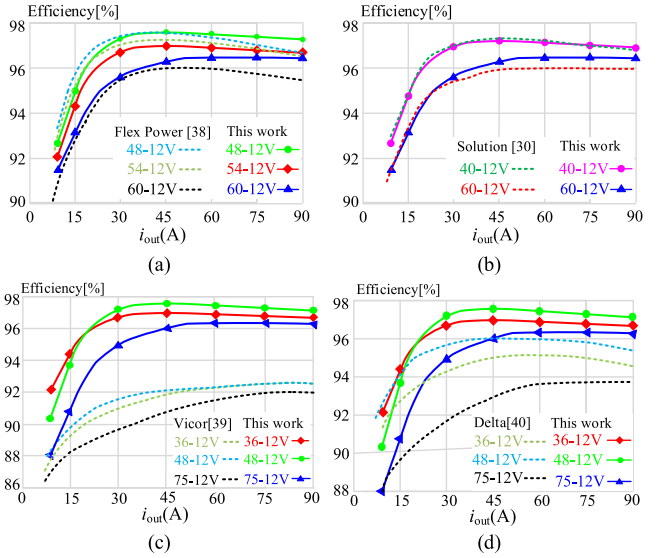


Fig. 29. Efficiency curves of converters at different input voltages. (a) Proposed converter and BMR4913208/857 of Flex Power. (b) Proposed converter and other state-of-the art solution [30]. (c) Proposed converter and DCM3623T75H13C2T of Vicor. (d) Proposed converter and E48SK12038NRDH of Delta.

much higher efficiency (peak of 96.3% at an input voltage of 60 V) and has a wider input voltage range.

The efficiency comparison curves of the proposed converter and other state-of-the art 12 V regulated *LLC* converter solutions [30] are shown in Fig. 29(b). With the same one-fourth brick footprint, the proposed converter can achieve much higher efficiency at input voltage of 40 V and 60 V. This is because the proposed converter adopts interleaved magnetic integration technology to obtain higher output voltage gain. Therefore, with variable input voltage away from the resonant frequency, the required working frequency and the loss are lower, and interleaved magnetic integration technology also reduces output ripple and noise, which can further improve efficiency.

The efficiency of the proposed converter is compared with that of the commercial power module DCM3623T75H13C2T and E48SK12038NRDH, and the results are shown in Fig. 29(c) and (d). DCM3623T75H13C2T, E48SK12038NRDH, and the proposed converter have the same input voltage range of 36–75 V. As shown in Fig. 29(c) and (d), under the same voltage and load current, the maximum efficiency of the proposed converter is 97.5%. It far exceeds DCM3623T75H13C2T (92.4%) and E48SK12038NRDH (96%). Apart from that, the proposed converter can maintain the efficiency above 96.5% from 20% to 100% loading conditions when input voltage is 36 V and 48 V. With the increase of the input voltage, when the input voltage is 75 V, the working frequency of the converter is away from the designed resonant frequency and the efficiencies of the three converters are greatly dropped. However, when the input voltage is 75 V, the overall efficiency of the proposed converter is maintained above 94% from 25% to 100% loading conditions, which is still far ahead of the efficiency of commercial power modules.

4) Table VIII summarizes the comprehensive performance comparison between the proposed converter and other state-of-the-art solutions and commercial products [30], [42], [43], [44]. In comparison to other solutions with a similar power density and efficiency [30], [42], the proposed converter has a wider input voltage range. Compared with commercial power modules with the same input voltage range of 36–75 V [43], [44], the proposed converter can achieve a higher maximum and full-load efficiency and a higher power density. Finally, the proposed converter can achieve the fastest transient response and the lowest output ripple and noise compared with all other state-of-the-art solutions .

In order to compare the comprehensive performance of each scheme more intuitively, based on Table VIII, a quantitative and

TABLE VIII
PERFORMANCE COMPARISON OF THIS STUDY WITH SOLUTIONS IN OTHER PIECES OF LITERATURE

| Parameter | This study | [30] | Flex Power [42] BMR4913208/857 | Vicor [43] DCM3623T75H13C2T | Delta [44] E48SK12038NRDH |
|---|---|---|---|---|---|
| Input voltage | 36–75 V | 40–60 V | 48–60 V | 36–75 V | 36–75 V |
| Output voltage | 12 V | 12 V | 12 V | 12 V | 12 V |
| Frequency | 0.75–1.6 MHz | 0.7–1.6 MHz | 0.18 MHz | 0.3–1MHz | 0.25 MHz |
| Max efficiency | 97.5% | 97.8% | 97.5% | 92.4% | 96% |
| Full-load efficiency | 97.2% | 97.6% | 96.6% | 91% | 95.1% |
| Max output power | 1080 W | 1000 W | 1540 W | 320 W | 450 W |
| Power density | 716 W/in$^3$ | 700 W/in$^3$ | 805 W/in$^3$ | 818 W/in$^3$ | 470 W/in$^3$ |
| Load transient current response | 11 A/$\mu$s (45 A–90 A)<br>9 A/$\mu$s (90 A–45 A) | - | 5 A/$\mu$s (45 A–90 A)<br>4.5 A/$\mu$s (90 A–45 A) | 4.5 A/$\mu$s (45 A–90 A)<br>4 A/$\mu$s (90 A–45 A) | 6.5 A/$\mu$s (45 A–90 A)<br>5.5 A/$\mu$s (90 A–45 A) |
| Load transient voltage deviation | 85 mV (45 A–90 A)<br>130 mV (90 A–45 A) | - | 145 mV (45 A–90 A)<br>155 mV (90 A–45 A) | 390 mV (45 A–90 A)<br>510 mV (90 A –45 A) | 690 mV (45 A–90 A)<br>720 mV (90 A–45 A) |
| Output ripple and noise | 40 mV | - | 60 mV | 100 mV | 450 mV |
| Max temperature | MOSFETs: 85 °C<br>Magnetic core: 88 °C | | MOSFETs: 79 °C<br>Magnetic core: 109 °C | 66 °C | MOSFETs: 68 °C<br>Magnetic core: 98 °C |
| Control method | Digital control<br>PFM | Digital control<br>PFM | Digital control<br>Hybrid regulation | Digital control<br>Sinusoidal amplitude regulation | Analog control<br>Pulsewidth modulation |
| Approach | Interleaving<br>Integrated magnetics<br>PCB winding<br>Si MOSFETs | Integrated<br>Magnetics<br>PCB winding<br>GaN | Matrix transformer<br>PCB winding<br>Si MOSFETs | Matrix transformer<br>PCB winding<br>Resonant drive<br>Si MOSFETs | Matrix transformer<br>PCB winding<br>Si MOSFETs |
| Cost | Medium | High | High | High | Low |

TABLE IX
QUANTITATIVE PERFORMANCE COMPARISON OF THIS WORK WITH OTHER-STATE-OF-THE-ART SOLUTIONS

| Converters | This study | Flex [42] | Vicor [43] | Delta [44] |
|---|---|---|---|---|
| Input voltage range | 36–75 V (PS = 6) | 48–60 V (PS = 3.5) | 36–75 V (PS = 6) | 36–75 V (PS = 6) |
| Efficiency | 97.5% (PS = 6) | 97.5% (PS = 6) | 92.4% (PS = 5.6) | 96% (PS = 5.9) |
| Power density | 716 W/in$^3$ (PS = 5.3) | 805 W/in$^3$ (PS = 5.9) | 818 W/in$^3$ (PS = 6) | 470 W/in$^3$ (PS = 3.4) |
| Transient response (load transient current response) (load transient voltage deviation) | 10 A/$\mu$s<br>108 mV (PS = 6) | 4.75 A/$\mu$s<br>150 mV (PS = 2.8) | 4.25 A/$\mu$s<br>450 mV (PS = 2.5) | 6 A/$\mu$s<br>705 mV (PS = 3.6) |
| Output ripple and noise | 40 mV (PS = 6) | 60 mV (PS = 4) | 100 mV (PS = 2.4) | 450 mV (PS = 0.5) |
| Temperature | 87.9 (PS = 4) | 82 (PS = 4.2) | 60 (PS = 6) | 80 (PS = 4.2) |
| Cost | Medium (PS = 4) | High (PS = 3) | High (PS = 2) | Low (PS = 6) |
| Total PS | 37.3 | 29.4 | 30.5 | 29.6 |

comprehensive comparison of different converter solutions is conducted and summarized in Table IX.

Table IX contains seven indicators, which are input voltage range, efficiency, power density, transient response, output ripple and noise, temperature, and cost, respectively. In this article, it is assumed that the above eight indicators are equally important in the comprehensive performance of the converter. On this basis, performance score (PS) is assigned to each indicator. In order to facilitate quantitative analysis, it is assumed that the maximum PS of each indicator is 6. Then, based on the above analysis and the experimental results in Table IX, the indices of each phase of each converter are normalized.

The ratio of the maximum input voltage to the minimum input voltage $V_{in\text{-}max}/V_{in\text{-}min}$ is used to represent the input voltage range of the converter. Thus, the maximum PS of input voltage range is 6. For the three indices, including output ripple and noise, temperature, and cost, this article adopts the reciprocal of the measured value to express the performance of the item. The higher the reciprocal value, the better the performance. Temperature in Table IX refers to the combined maximum temperature of the inductor, transformer, and MOSFETs. Moreover, transient response in Table IX refers to the comprehensive performance of the load transient current response speed and the load transient voltage deviation when the load step is between 45 and 90 A.

The cost in Table IX is determined by considering the design difficulty of topology, cost of designing, and manufacturing integrated magnetic components and PCB windings, as well as the cost of power devices and control. The E48SK12038NRDH of Delta uses only matrix transformer and PCB winding design and adopts Si MOSFETs and simple analog control. Thus, it is assumed to have the lowest cost and the corresponding PS of cost is 6. Based on the above technical approach, commercial power products BMR4913208/857 and DCM3623T75H13C2T adopt the patented HRR topology and SAC topology, respectively. In addition, DCM3623T75H13C2T also uses complex and expensive CHIP technology, as well as resonant drive technology. Therefore, the cost of BMR4913208/857 and DCM3623T75H13C2T is high, and the corresponding PS of cost is 3 and 2, respectively.

In summary, the total PS of the proposed converter is the highest. In order to intuitively compare the comprehensive performance of the proposed converter and other state-of-the-art solutions, a comprehensive performance comparison diagram, as shown in Fig. 30, is drawn based on the PS comparison results in Table IX. The quantitative analysis and comparison verify that

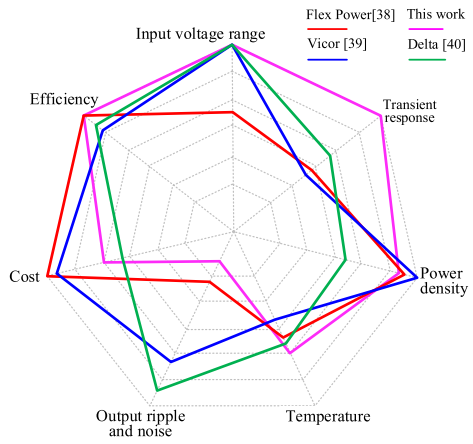


Fig. 30. Comparison of different 12 V regulated isolated DC–DC converter solutions.

the proposed converter has significant advantages in terms of the comprehensive performance.

## V. Conclusion

This article presents a new high efficiency, low ripple, and high dynamic response multiphase interleaved magnetic integrated *LLC* converter for wide input voltage bus converter. Moreover, the proposed ICRI improves the sensitivity of the gain response to frequency variation. On the basis of maintaining the advantages of the size, efficiency, and soft switching of the multiphase *LLC* converter, it can not only expand the gain range but also realize the active current sharing. Furthermore, this article puts forward a magnetic circuit modeling method based on the parallel ICRI, which considers the edge effect of air gaps magnetic field and the leakage flux outside the windings. It turns out that the method is accurate and universal. Finally, the proposed converter has an output power of 1080 W (12 V, 90 A), a maximum efficiency of 97.5%, and a power density of 716 W/in$^3$. According to the quantitative performance comparison results, the proposed converter is superior to other solutions in terms of the comprehensive performance.

## References

[1] C. Fei, F. C. Lee, and Q. Li, "High-efficiency high-power-density LLC converter with an integrated planar matrix transformer for high-output current applications," *IEEE Trans. Ind. Electron.*, vol. 64, no. 11, pp. 9072–9082, Nov. 2017.

[2] S. S. Rao and G. Amer, "Power supply architecture for telecom application: A review," in *Proc. Int. Conf. Commun. Control Comput. Technol.*, 2010, pp. 262–264.

[3] U. Kundu, K. Yenduri, and P. Sensarma, "Accurate ZVS analysis for magnetic design and efficiency improvement of full-bridge LLC resonant converter," *IEEE Trans. Power Electron.*, vol. 32, no. 3, pp. 1703–1706, Mar. 2017.

[4] J.-B. Lee, J.-K. Kim, J.-H. Kim, J.-I. Baek, and G.-W. Moon, "A high-efficiency PFM half-bridge converter utilizing a half-bridge LLC converter under light load conditions," *IEEE Trans. Power Electron.*, vol. 30, no. 9, pp. 4931–4942, Sep. 2015.

[5] X. Fang, H. Hu, Z. J. Shen, and I. Batarseh, "Operation mode analysis and peak gain approximation of the LLC resonant converter," *IEEE Trans. Power Electron.*, vol. 27, no. 4, pp. 1985–1995, Apr. 2012.

[6] L. Wang, D. Zhang, Y. Yang, and H. Li, "Two-stage factorized power architecture DC–DC converter for spacecraft secondary power supply system," *IEEE J. Emerg. Sel. Topics Power Electron.*, vol. 10, no. 5, pp. 5392–5413, Oct. 2022, doi: 10.1109/JESTPE.2022.3140431.

[7] M. H. Ahmed, C. Fei, F. C. Lee, and Q. Li, "Single-stage high-efficiency 48/1 V sigma converter with integrated magnetics," *IEEE Trans. Ind. Electron.*, vol. 67, no. 1, pp. 192–202, Jan. 2020.

[8] Y. Chen et al., "LCLC converter with optimal capacitor utilization for hold-up mode operation," *IEEE Trans. Power Electron.*, vol. 34, no. 3, pp. 2385–2396, Mar. 2019.

[9] D.-K. Kim, S. Moon, C.-O. Yeon, and G.-W. Moon, "High-efficiency LLC resonant converter with high voltage gain using an auxiliary LC resonant circuit," *IEEE Trans. Power Electron.*, vol. 31, no. 10, pp. 6901–6909, Oct. 2016.

[10] W. Inam, K. K. Afridi, and D. J. Perreault, "High efficiency resonant DC/DC converter utilizing a resistance compression network," *IEEE Trans. Power Electron.*, vol. 29, no. 8, pp. 4126–4135, Aug. 2014.

[11] D. Huang, F. C. Lee, and D. Fu, "Classification and selection methodology for multi-element resonant converters," in *Proc. 26th Annu. IEEE Appl. Power Electron. Conf. Expo.*, 2011, pp. 558–565.

[12] X. Sun, Y. Shen, Y. Zhu, and X. Guo, "Interleaved boost-integrated LLC resonant converter with fixed-frequency PWM control for renewable energy generation applications," *IEEE Trans. Power Electron.*, vol. 30, no. 8, pp. 4312–4326, Aug. 2015.

[13] R. Beiranvand, M. R. Zolghadri, B. Rashidian, and S. M. H. Alavi, "Optimizing the LLC–LC resonant converter topology for wide-output-voltage and wide-output-load applications," *IEEE Trans. Power Electron.*, vol. 26, no. 11, pp. 3192–3204, Nov. 2011.

[14] K.-H. Yoon, Y.-J. Noh, S. Phum, S. Meas, S.-H. Jang, and E.-S. Kim, "LLC resonant converter with wide input voltage and load range at fixed switching frequency," in *Proc. 27th Annu. IEEE Appl. Power Electron. Conf. Expo.*, 2012, pp. 1338–1342.

[15] H. Hu, X. Fang, F. Chen, Z. J. Shen, and I. Batarseh, "A modified high-efficiency LLC converter with two transformers for wide input-voltage range applications," *IEEE Trans. Power Electron.*, vol. 28, no. 4, pp. 1946–1960, Apr. 2013.

[16] H. Wang, Y. Chen, P. Fang, Y. Liu, J. Afsharian, and Z. Yang, "An LLC converter family with auxiliary switch for hold-up mode operation," *IEEE Trans. Power Electron.*, vol. 32, no. 6, pp. 4291–4306, Jun. 2017.

[17] M. M. Jovanović and B. T. Irving, "On-the-fly topology-morphing control—Efficiency optimization method for LLC resonant converters operating in wide Input- and/or output-voltage range," *IEEE Trans. Power Electron.*, vol. 31, no. 3, pp. 2596–2608, Mar. 2016.

[18] M. I. Shahzad, S. Iqbal, and S. Taib, "Interleaved LLC converter with cascaded voltage-doubler rectifiers for deeply depleted PEV battery charging," *IEEE Trans. Transp. Electrific.*, vol. 4, no. 1, pp. 89–98, Mar. 2018.

[19] K. Jin and X. Ruan, "Hybrid full-bridge three-level LLC resonant converter—A novel DC–DC converter suitable for fuel-cell power system," *IEEE Trans. Ind. Electron.*, vol. 53, no. 5, pp. 1492–1503, Oct. 2006.

[20] Z. Hu, Y. Qiu, Y.-F. Liu, and P. C. Sen, "A control strategy and design method for interleaved LLC converters operating at variable switching frequency," *IEEE Trans. Power Electron.*, vol. 29, no. 8, pp. 4426–4437, Aug. 2014.

[21] K. Murata and F. Kurokawa, "An interleaved PFM LLC resonant converter with phase-shift compensation," *IEEE Trans. Power Electron.*, vol. 31, no. 3, pp. 2264–2272, Mar. 2016.

[22] H. Wang, Y. Chen, Y.-F. Liu, J. Afsharian, and Z. Yang, "A passive current sharing method with common inductor multiphase LLC resonant converter," *IEEE Trans. Power Electron.*, vol. 32, no. 9, pp. 6994–7010, Sep. 2017.

[23] H. Wang et al., "Common capacitor multiphase LLC converter with passive current sharing ability," *IEEE Trans. Power Electron.*, vol. 33, no. 1, pp. 370–387, Jan. 2018.

[24] Y. Yang, J. Yao, H. Li, and J. Zhao, "A novel current sharing method by grouping transformer's secondary windings for a multiphase LLC resonant converter," *IEEE Trans. Power Electron.*, vol. 35, no. 5, pp. 4877–4890, May 2020.

[25] C. Fei, R. Gadelrab, Q. Li, and F. C. Lee, "High-frequency three-phase interleaved LLC resonant converter with GaN devices and integrated planar magnetics," *IEEE J. Emerg. Sel. Topics Power Electron.*, vol. 7, no. 2, pp. 653–663, Jun. 2019.

[26] R. Gadelrab, F. C. Lee, and Q. Li, "Three-phase interleaved LLC resonant converter with integrated planar magnetics for telecom and server application," in *Proc. IEEE Appl. Power Electron. Conf. Expo.*, 2020, pp. 512–519.

[27] B. Li, Q. Li, and F. C. Lee, "Phase shading for light load efficiency improve in three-phase resonant converter with integrated PCB winding magnetics," in *Proc. 10th Int. Conf. Power Electron. ECCE Asia*, 2019, pp. 2362–2367.
[28] B. Li, Q. Li, and F. C. Lee, "A WBG based three phase 12.5 kW 500 kHz CLLC resonant converter with integrated PCB winding transformer," in *Proc. IEEE Appl. Power Electron. Conf. Expo.*, 2018, pp. 469–475.
[29] L. Shi, B. Liu, and S. Duan, "Current sharing method based on optimal phase shift control for interleaved three-phase half bridge LLC converter with floating Y-connection," *J. Power Electron.*, vol. 19, no. 4, pp. 934–943, Jul. 2019.
[30] M. H. Ahmed, A. Nabih, F. C. Lee, and Q. Li, "Low-loss integrated inductor and transformer structure and application in regulated LLC converter for 48-V bus converter," *IEEE J. Emerg. Sel. Topics Power Electron.*, vol. 8, no. 1, pp. 589–600, Mar. 2020.
[31] X. Wu and H. Shi, "High efficiency high density 1 MHz 380–12 V DCX with low FoM devices," *IEEE Trans. Ind. Electron.*, vol. 67, no. 2, pp. 1648–1656, Feb. 2020.
[32] L. Wang, D. Zhang, J. Duan, and J. Li, "High-frequency symmetric multiphase array CIs for interleaved bidirectional DC-DC converters," in *Proc. IEEE 13th Conf. Ind. Electron. Appl.*, 2018, pp. 204–209.
[33] Y. Yang and S. Dai, "Design criterion for asymmetric CIs in interleaving & magnetically integrated bidirectional DC/DC converter," in *Proc. IEEE 2nd Int. Future Energy Electron. Conf.*, 2015, pp. 1–11.
[34] C. Fei, F. C. Lee, and Q. Li, "A new design paradigm for GaN based LLC converter," in *Proc. IEEE Southern Power Electron. Conf.*, 2017, pp. 1–6, doi: 10.1109/SPEC.2017.8333548.
[35] D. Fu, F. C. Lee, and S. Wang, "Investigation on transformer design of high frequency high efficiency dc-dc converters," in *Proc. 25th Annu. IEEE Appl. Power Electron. Conf. Expo.*, 2010, pp. 940–947.
[36] Y. Yang, T. Guan, S. Zhang, W. Jiang, and W. Huang, "More symmetric four-phase inverse coupled inductor for low current ripples & high-efficiency interleaved bidirectional buck/boost converter," *IEEE Trans. Power Electron.*, vol. 33, no. 3, pp. 1952–1966, Mar. 2018.
[37] A. Balakrishnan, W. T. Joines, and T. G. Wilson, "Air-gap reluctance and inductance calculations for magnetic circuits using a Schwarz–Christoffel transformation," *IEEE Trans. Power Electron.*, vol. 12, no. 4, pp. 654–663, Jul. 1997.
[38] J. E. Fletcher, B. W. Williams, and M. M. Mahmoud, "Air gap fringing flux reduction in inductors using open-circuit copper screens," *IEE Proc. Electr. Power Appl.*, vol. 152, no. 4, pp. 990–996, Jul. 2005.
[39] 2016. [Online]. Available: http://www.chinadmegc.com/products_list.php?2
[40] M. Fu, C. Fei, Y. Yang, Q. Li, and F. C. Lee, "Optimal design of planar magnetic components for a two-stage GaN-based DC–DC converter," *IEEE Trans. Power Electron.*, vol. 34, no. 4, pp. 3329–3338, Apr. 2019.
[41] Y. Cai, M. H. Ahmed, Q. Li, and F. C. Lee, "Optimized design of integrated PCB-winding transformer for MHz LLC converter," in *Proc. IEEE Appl. Power Electron. Conf. Expo.*, 2019, pp. 1452–1458.
[42] Flex Power, "BMR491 series 2450 w peak power 1/4 brick DC/DC converter input 48–60 V, output up to 128 A/1540 W datasheet," Nov. 2021. [Online]. Available: https://flexpowermodules.com/products/bmr491?model=BMR491XX08%2F857
[43] Vicor, "Isolated digital regulated DC/DC converter input voltage 36–75 V, output power up to 26.67 A/320 W datasheet," Nov. 2021. [Online]. Available: https://www.vicorpower.com/documents/datasheets/DCM3623x75H13C2yzz_ds.pdf
[44] "Delta electronics, E48SK12038NRDH series 450 W power 1/8 brick DC/DC converter input 36–75 V, output up to 37.5 A/450 W datasheet," Nov. 2021. [Online]. Available: https://www.deltaww.com/en-US/Products/010201010104/ALL/

**Lei Wang** was born in Anhui, China, in 1991. He received the B.S. and M.S. degrees from Liaoning Technology University, Huludao, China, in 2014 and 2016, respectively. He is currently working toward the Ph.D. degree in power electronics and power drives with the Harbin Institute of Technology, Shenzhen, China.

He joined Delta Electronic Enterprise Management (Shanghai) Co., Ltd., in August 2016, as a Senior Electronic Designer. His current research interests include magnetic integration in power electronics converters and aerospace power technology.

**Donglai Zhang** (Senior Member, IEEE) was born in Jilin, China, in 1973. He received the B.S., M.S., and Ph.D. degrees from the Harbin Institute of Technology, Harbin, China, in 1994, 1996, and 1999, respectively.

Since 2005, he has been a Professor with the Harbin Institute of Technology (Shenzhen), Shenzhen, China. His research interests include analysis, modeling, and control of power converters, digital control techniques for power electronic circuits, and grid-connected converters for renewable energy systems. In these research fields, he was leading several industrial and government projects. He is a Senior Member of China Power Electronics Society.

**Jinpei Duan** was born in Henan, China, in 1994. He received the B.S. degree from Yanshan University, Qinhuangdao, China, in 2017. He is currently working toward the Ph.D. degree in power electronics and power drives with the Harbin Institute of Technology, Shenzhen, China.

His research interests include power electronics system integration, dynamic modeling, and control design.

**Yangyang Hao** was born in Hunan, China, in 1995. He received the undergraduate degree in electrical engineering and automation and the master's degree in control science and engineering from the School of Automation, Qingdao University of Technology, Qingdao, China, in 2017 and 2021 respectively.

He is currently an Engineering Doctor in the energy and power discipline with the School of Electromechanical and Information Engineering, Harbin Institute of Technology (Shenzhen), Shenzhen, China. My research direction is new power converter topology and electric propulsion power supply.